AFRL-AFOSR-VA-TR-2020-0041

DESIGN OF NEW PIEZOELECTRIC COMPOSITES USING NANOCELLULOSE

Seong Kim
PENNSYLVANIA STATE UNIVERSITY

08/29/2019
Final Report

Air Force Research Laboratory
AF Office Of Scientific Research (AFOSR)/ RTA1
Arlington, Virginia 22203
Air Force Materiel Command

REPORT DOCUMENTATION PAGE

Form Approved
OMB No. 0704-0188

1. REPORT DATE *(DD-MM-YYYY)*	2. REPORT TYPE	3. DATES COVERED *(From - To)*
21-05-2020	Final Performance	01 Dec 2015 to 31 May 2019

4. TITLE AND SUBTITLE
DESIGN OF NEW PIEZOELECTRIC COMPOSITES USING NANOCELLULOSE

5a. CONTRACT NUMBER

5b. GRANT NUMBER
FA9550-16-1-0062

5c. PROGRAM ELEMENT NUMBER
61102F

6. AUTHOR(S)
Seong Kim

5d. PROJECT NUMBER

5e. TASK NUMBER

5f. WORK UNIT NUMBER

7. PERFORMING ORGANIZATION NAME(S) AND ADDRESS(ES)
PENNSYLVANIA STATE UNIVERSITY
201 OLD MAIN
UNIVERSITY PARK, PA 16802-1505 US

8. PERFORMING ORGANIZATION REPORT NUMBER

9. SPONSORING/MONITORING AGENCY NAME(S) AND ADDRESS(ES)
AF Office of Scientific Research
875 N. Randolph St. Room 3112
Arlington, VA 22203

10. SPONSOR/MONITOR'S ACRONYM(S)
AFRL/AFOSR RTA1

11. SPONSOR/MONITOR'S REPORT NUMBER(S)
AFRL-AFOSR-VA-TR-2020-0041

12. DISTRIBUTION/AVAILABILITY STATEMENT
A DISTRIBUTION UNLIMITED: PB Public Release

13. SUPPLEMENTARY NOTES

14. ABSTRACT

This research project focused on cellulose crystals as building blocks for the design and development of new low-density functional polymer composites. Although the piezoelectricity of cellulose has been predicted from its noncentrosymmetric crystal structure, it has not been measured accurately nor has cellulose been properly exploited as a piezoelectric material. If it is proven, it could enable novel low-density electroactive materials capable of surpassing the performance of the best synthetic piezoelectric polymer such as polyvinylidene difluoride (PVDF). To fulfill this objective, a systematic study was required to judiciously manipulate dipoles of individual cellulose nanocrystals to produce polar ordering at the macroscale. With the unique capability of spectroscopically determining the degree of polar ordering of cellulose in the sample using vibrational sum frequency generation (SFG) spectroscopy, we found that none of the previously used methods for preparation of cellulose-containing piezoelectric materials really produces any polar ordering. Thus, what was reported as a piezoelectric response of cellulose in the literature cannot be attributed to piezoelectricity; we found that what was reported falls under electromechanical coupling originating from other extrinsic mechanisms. The question regarding the intrinsic piezoelectricity of cellulose remains to be answered; the intrinsic piezoelectric coefficient of cellulose appears to be very small. While exploring the directional alignment of cellulose, we have demonstrated that (a) SFG is a quantitative tool to determine the polar ordering, (b) in the LB trough, cellulose nanoparticles can topographically corrugate liquid/surfactant/air interface, (c) the capillary flow of the fluid phase during the LB transfer can improve the uniaxial alignment of anisotropic nanoparticles onto a substrate, and (d) magnetic

15. SUBJECT TERMS
PIEZOELECTRIC COMPOSITES, Piezoelectric Nanocellulose, Electroactive materials

Standard Form 298 (Rev. 8/98)
Prescribed by ANSI Std. Z39.18

16. SECURITY CLASSIFICATION OF:			17. LIMITATION OF ABSTRACT	18. NUMBER OF PAGES	19a. NAME OF RESPONSIBLE PERSON
a. REPORT	b. ABSTRACT	c. THIS PAGE			TILEY, JAIMIE
Unclassified	Unclassified	Unclassified	UU		19b. TELEPHONE NUMBER *(Include area code)* 703-588-8316

Final Report of Grant FA9550-16-1-0062

Grant title: DESIGN OF NEW PIEZOELECTRIC COMPOSITES USING NANOCELLULOSE

PIs: Seong H. Kim & Zoubeida Ounaies (Pennsylvania State University)

Program manager: Dr. J. Tiley

Program: Low density materials

Synopsis

This research project focused on cellulose crystals as building blocks for the design and development of new low-density functional polymer composites. Although the piezoelectricity of cellulose has been predicted from its noncentrosymmetric crystal structure, it has not been measured accurately nor has cellulose been properly exploited as a piezoelectric material. If it is proven, it could enable novel low-density electroactive materials capable of surpassing the performance of the best synthetic piezoelectric polymer such as polyvinylidene difluoride (PVDF). To fulfill this objective, a systematic study was required to judiciously manipulate dipoles of individual cellulose nanocrystals to produce polar ordering at the macroscale and accurately characterize the nano-to-mesoscale structural ordering and electromechanical properties of the produced materials.

Based on its noncentrosymmetric crystal structure, nanocrystalline cellulose has been assumed to be piezoelectric; but it has not been properly or convincingly characterized in the literature. The key obstacle is that nanoscale piezoelectric properties of individual crystals cancel each other when cellulose crystals are dispersed randomly or when they are assembled into simple uniaxial structures in which most cellulose particles are packed in the antiparallel fashion in average. Overcoming this obstacle could accelerate the realization of cellulose-based piezoelectric materials and related applications. With this premise, our team with multidisciplinary experimental backgrounds explored various ways of inducing polar ordering (i.e., parallel packing) of nanocrystalline cellulose domains. The methods tested included (i) chemical derivatizations followed by Langmuir-Blodgett (LB) film deposition, (ii) electric field (both DC and AC) induced orientation of cellulose dipoles, and (iii) magnetic field induced orientation using the diamagnetic property of cellulose. With the unique capability of spectroscopically determining the degree of polar ordering of cellulose in the sample using vibrational sum frequency generation (SFG) spectroscopy and other complementary techniques, we found that none of these methods, which were previously used and reported for preparation of cellulose-containing piezoelectric materials in the literature, really produces any polar ordering. Thus, what was reported as a piezoelectric response of

cellulose in the literature cannot be attributed to piezoelectricity; we found that what was reported falls under electromechanical coupling originating from other mechanisms that are not intrinsic to the noncentrosymmetric cellulose crystal structure. Those mechanisms were found to originate from extrinsic factors such as electrochemical or interfacial polarization within the composite samples containing cellulose nanocrystals. Thus, the question regarding the intrinsic piezoelectricity of cellulose remains to be answered; the intrinsic piezoelectric coefficient of cellulose appears to be very small, although we could not determine the absolute value in this study. While exploring the directional alignment of cellulose, we have demonstrated that (a) SFG is indeed a quantitative tool to determine the polar ordering of molecular functional groups in the sample, (b) in the LB trough, cellulose nanoparticles can topographically corrugate liquid/surfactant/air interface, (c) the capillary flow of the fluid phase during the LB transfer can improve the uniaxial alignment of anisotropic nanoparticles onto a substrate, and (d) magnetic-field induced ordering of cellulose suspended in liquids is a function of dielectric constant, ion conductivity, and viscosity of the suspension solution. These research findings further expand potential applications of cellulose nanoparticles in various engineering applications.

In terms of dissemination, this project resulted in 7 published and submitted (or ready to submit) journal papers, one conference proceedings paper and 10 conference presentations from which 6 were invited presentations.

Participants

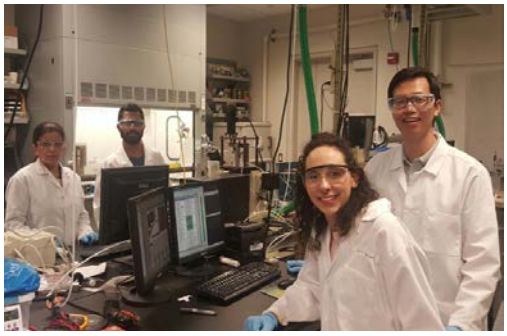

Researchers who contributed to this project are pictured here. From left to right: Dr. A. Meddeb, Dr. N. D'Souza, Ms. N. Rome, and Mr. I. Chae.

In addition to the PIs Kim and Ounaies, four dedicated researchers have been involved in this project. Inseok Chae is a PhD student in the Department of Chemical Engineering at Penn State. He joined our team in January 2016 after he had obtained his master's degree at University of Alberta in Canada. Dr. Amira B. Meddeb, an associate research professor in the Department of Mechanical Engineering at Penn State, has worked on this project since November 2017. Prior to that, Dr. Hassene Ben Atitallah (currently at Seagate) and Dr. Noel D'Souza (currently at Intel) had worked in our team for 7 months and 13 months, respectively. Additionally, Amy Tomasko (an undergraduate student in chemical engineering

at Penn State) and Natalie Rome (an undergraduate student from University of Louisiana, Lafayette, NSF-funded REU program) have contributed to this research as well.

Task Accomplishments

The five main objectives (OBJ) of this project are as follows:

OBJ #1: critical review of electromechanical coupling responses of cellulose in literature

OBJ #2: selective detection of polar domains of cellulose using vibrational SFG spectroscopy

OBJ #3: dispersion of individual cellulose nanocrystals (CNCs) in organic solvents and polymer matrix

OBJ #4: understanding translational and rotational behaviors of CNCs under external fields/forces

OBJ #5: construction of nano-building blocks of CNCs with uniaxial alignment using LB method and investigation of their optical and frictional anisotropic properties

Table 1 summarizes the detailed methods and achievements on each objective. There are tasks already completed (blue) and abandoned due to the technical limits (red).

Table 1. Summary of achievements

OBJ	Tasks	Methods	Results	Conclusion/Plan
#1	critical review of electromechanical coupling responses of cellulose in literature	literature review	elucidated non-piezoelectric responses which can affect piezoelectric measurements of cellulose	completed, published[1]
#2	selective detection of polar domains of cellulose using vibrational SFG spectroscopy	proof of concept: *in-situ* SFG measurement of PVDF upon poling	successful quantification of polar ordering of piezoelectric polymer, PVDF	completed, published[2]
		TD-DFT calculation of SFG spectra of cellulose	obtained theoretical and experimental SFG feature of parallel and anti-parallel cellulose	completed, published[3]
		SFG and dielectric measurement of EAPap	identified non-polar ordering and extrinsic electromechanical responses of EAPap	completed, to be included in the PhD thesis of Inseok Chae
#3	dispersion of individual CNCs in organic solvents and polymer matrix	solvent exchange from water to organic solvents, then embed in a polymer matrix	individual dispersions were achieved using ethanol, NMF, DMF and PVAC	completed, to be included in the PhD thesis of Inseok Chae
		coating cationic or non-ionic surfactants on CNCs	Caused aggregation of CNCs in water and toluene	abandoned

		solvent exchange to non-polar organic solvents	Caused aggregation of CNCs in THF and toluene	abandoned
#4	understanding translational and rotational behaviors of CNCs under external fields/forces	apply compression or stretching on CNCs	uniaxial, but anti-parallel alignment of CNCs was achieved	completed, submitted[4]
		apply AC or DC electric field on CNCs	AC: non-homogeneous alignments of CNCs DC: translation due to surface charge >> rotation due to dipole interaction	completed, to be included in the PhD thesis of Inseok Chae
		apply magnetic field on CNCs	enhanced chiral nematic phase of CNCs, but in anti-parallel fashion	completed, submitted/preparation[5-6]
#5	construction of nanobuilding blocks of CNCs with uniaxial alignment using LB method and investigation of their optical and frictional anisotropic properties	compression- and flow-induced alignment of CNCs in LB deposition	developed an effective method to prepare uniaxially aligned CNCs. optical and frictional anisotropic properties of CNCs were obtained.	completed, submitted[7]

Abbreviations: cellulose nanocrystal (CNC), tetrahydrofuran (THF), dimethylformamide (DMF), N-methylformamide (NMF), polyvinyl acetate (PVAC), Langmuir-Blodgett (LB), sum frequency generation (SFG), polyvinylidene fluoride (PVDF), piezoelectric force microscopy (PFM), electro active paper (EAPap), time-dependent density functional theory (TD-DFT)

Publications

1. Chae, I.; Jeong, C. K.; Ounaies, Z.; Kim, S. H., Review on Electromechanical Coupling Properties of Biomaterials. *ACS Applied Bio Materials* **2018,** *1* (4), 936-953. doi: 10.1021/acsabm.8b00309
2. Chae, I.; Ahmed, S.; Atitallah, H. B.; Luo, J.; Wang, Q.; Ounaies, Z.; Kim, S. H., Vibrational Sum Frequency Generation (SFG) Analysis of Ferroelectric Response of Pvdf-Based Copolymer and Terpolymer. *Macromolecules* **2017,** *50* (7), 2838-2844. doi: 10.1021/acs.macromol.7b00188
3. Lee, C. M.; Chen, X.; Weiss, P. A.; Jensen, L.; Kim, S. H., Quantum Mechanical Calculations of Vibrational Sum-Frequency-Generation (SFG) Spectra of Cellulose: Dependence of the Ch and Oh Peak Intensity on the Polarity of Cellulose Chains within the SFG Coherence Domain. *J. Phys. Chem. Lett.* **2017,** *8* (1), 55-60. doi: 10.1021/acs.jpclett.6b02624
4. Chae, I.; Ngo, D.; Makarem, M.; Ounaies, Z.; Kim, S. H., Compression-Induced Topographic Corrugation of Air/Surfactant/Water Interface: Effect of Nanoparticles Adsorbed beneath the Interface. *In revision, J. Phys. Chem. C.*
5. Meddeb, A. B.; Chae, I.; Aijie, H.; Kim, S. H.; Ounaies, Z., Solvent Properties, Particle Content and Magnetic Field Effects on Cellulose Nanocrystals Packing in Suspensions. *Submitted to ACS Applied Bio Materials*.
6. Meddeb, A. B.; Chae, I.; Kim, S. H.; Ounaies, Z., Enhanced Antiparallel Packing of Cellulose Nanocrystals by Magnetic Field Application. *Manuscript in preparation*.
7. Chae, I.; Ngo, D.; Chen, Z.; Meddeb, A. B.; Kwansa, A.; Podraza, N. J.; Yingling, Y. G.; Ounaies, Z.; Kim, S. H., Structuring of Rod-Shaped Nanoparticles in Langmuir-Blodgett Film: Effect of Uniaxial Alignment of Optical and Frictional Anisotropy. *Submitted to ACS Applied Materials & Interfaces.*

Conferences

1. American Chemical Society (ACS) National Meeting in Orlando, **2019**
   Presentation: Piezoelectricity of Cellulose: Myths and Facts, by Seong H. Kim
2. American Society of Mechanical Engineering-SMASIS in San Antonio, **2018**

Proceeding: Chae, I.; Meddeb, A.B.; Ounaies, Z.; Kim, S. H.; Tailoring and Characterization of the Liquid Crystalline Structure of Cellulose Nanocrystals for Opto-Electro-Mechanical Multifunctional Applications. *SMASIS2018-8016*. doi: 10.1115/SMASIS2018-8016
Presentation: Tailoring and Characterization of the Liquid Crystalline Structure of Cellulose Nanocrystals for Opto-Electro-Mechanical Multifuntional Applications, by Inseok Chae

3. ACS National Meeting in Boston, **2018**
   Presentation: Critical Discussion of Electromechanical Coupling Properties of Cellulose, by Inseok Chae
4. ACS colloid & Surface Science Symposium, University Park, **2018**
   Presentation: Phase and Orientation Control of Cellulose Nanocrystals by Langmuir-Blodgett Assembly, by Inseok Chae
5. Department of Mechanical Engineering Seminar Series, Florida State University, Tallahassee, FL, "Multi-field processing of anisotropic nanoparticles for multifunctional applications," Invited. (April 25, 2018), by Z. Ounaies.
6. Korean Aerospace University (KAU), Goyang, South Korea, "Active polymer composites: Structure-processing-processing triad," Invited. (April 3, 2018). by Z. Ounaies.
7. Sungkyunkwan University (SKKU), Suwon, Korea, "Responsive polymer-based materials: Processing, characterization and oppurtunities," Invited. (April 2, 2018). by Z. Ounaies.
8. Inha University, Incheon, Korea, "Multi-field processing of anisotropic nanoparticles for multifunctional applications," Invited. (March 29, 2018). By Ounaies, Z.
9. Air Force Office of Scientific Research (AFOSR) Student Research Day in Arlington, **2017**
   Presentation: Design of New Piezoelectric Composites Using Nanocellulose, by Inseok Chae
10. Materials day at Penn State, University Park, **2016-2017**
    Presentation (2016): Understanding the Structure, Interface Interactions and Piezoelectric Properties of Cellulose Using Nonlinear Spectroscopy, by Inseok Chae
    Presentation (2017): Understanding the Native Assembly, Interface Interactions and Piezoelectric Properties of Cellulose Using SFG Vibrational Spectroscopy, by Inseok Chae

1. Critical review of electromechanical coupling responses of cellulose in literature

Electromechanical coupling is a phenomenon where an electrical charge is produced when mechanical force is applied to a material or mechanical strain is generated under electric field. The most well-known mechanism is piezoelectricity. The piezoelectricity of cellulose has been reported since 1950s with many potential applications such as biocompatible sensors and actuators, and ecofriendly energy harvesters; however, the accurate values of piezoelectric properties has not been identified, yet. Without identifying the exact values, it is not possible to practically use the piezoelectricity of cellulose. Fig. 1 shows the selected piezoelectric coefficients of cellulose from literatures. Different from well-defined piezoelectricity of PZT and PVDF, the piezoelectric coefficients of cellulose in the literature scatter over several orders of magnitude. The fact that the values scatter over an extremely wide range raises the question of whether these reported values are truly intrinsic piezoelectric properties of cellulose or whether they are obscured with other electromechanical coupling processes.

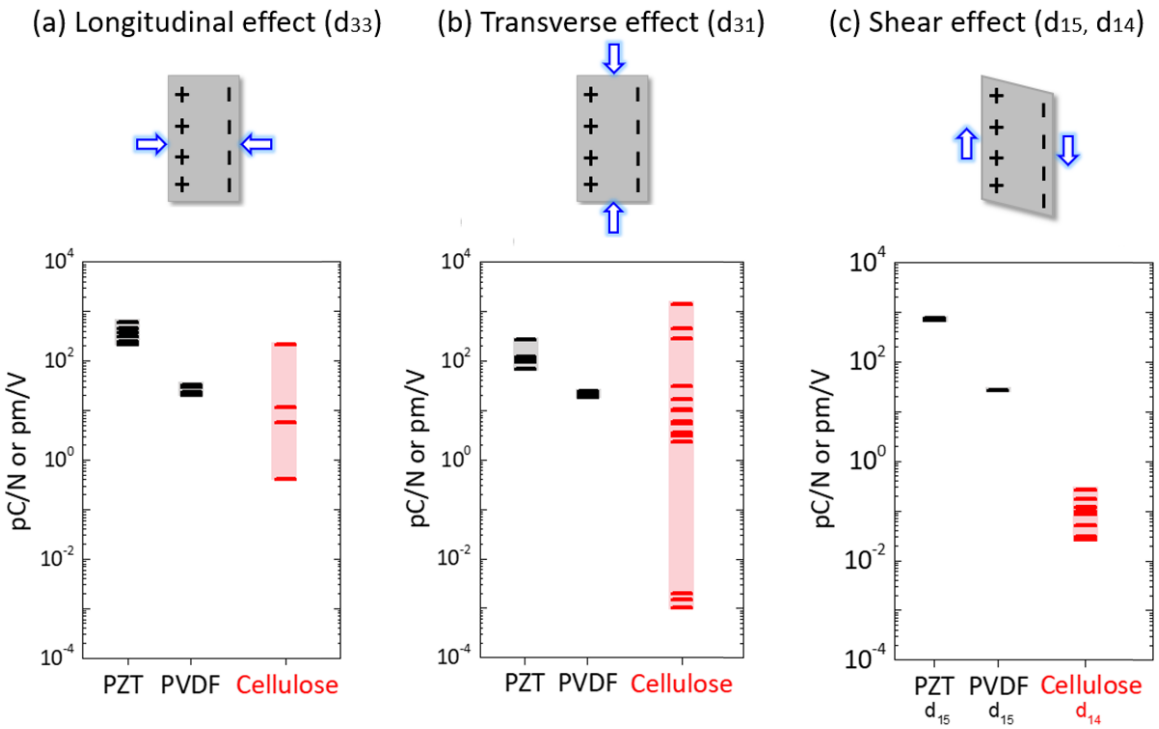

Figure 1. (a) Longitudinal, (b) transverse and (c) shear piezoelectric coefficients of cellulose-based biomaterials reported in literature.[1, 8-38] The piezoelectric coefficients of PZT and PVDF were included for comparisons. Blue arrows in the schematics represent the applied stress.

Piezoelectricity is not the only electromechanical coupling phenomenon; there are other mechanisms which convert mechanical energy to electrical energy or vice versa such as electrostriction and flexoelectricity as shown in Fig. 2. Also, extrinsic factors including electrochemical and electrostatic effects can contribute to electromechanical signals. In some cases, these non-piezoelectric couplings are misconstrued as inherent piezoelectric responses, depending on a sample preparation or experimental set up. Without filtering out these non-piezoelectric couplings, it is difficult to obtain quantitative values of piezoelectric properties.

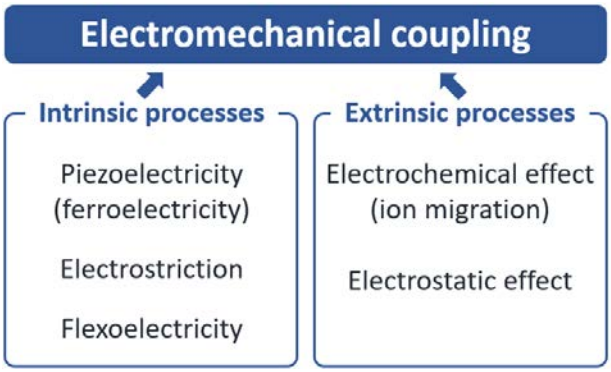

Figure 2. Diagram of electromechanical coupling phenomena with the intrinsic and extrinsic processes.[1]

In order to elucidate the true piezoelectricity of biomaterials, the relationship between polar domains and piezoelectric properties should be identified since the arrangement of polar domains govern the piezoelectricity. Fig. 3 shows the schematics of this relationship. The piezoelectricity can be maximized in the geometry where polar domains (arrows) are arranged in a parallel manner; however, it can be minimized or cancelled due to the symmetry cancellation when the polar domains are arranged in random or anti-parallel. Even though individual CNCs are predicted to have the piezoelectric properties, the piezoelectric behavior cannot be seen in a macroscopic scale if they are arranged in random or anti-parallel. Therefore, *an effective method to align the CNCs in parallel is required to identify their piezoelectricity. It is a challenging task since random or anti-parallel arrangements are entropically more favorable than the ordered geometry.* Also, many land plants have been studied to have anti-parllel or random arrangement; no clear evidence of parallel arrangement of cellulose crystals in natural samples or engineered composites have not been reported, yet.[1]

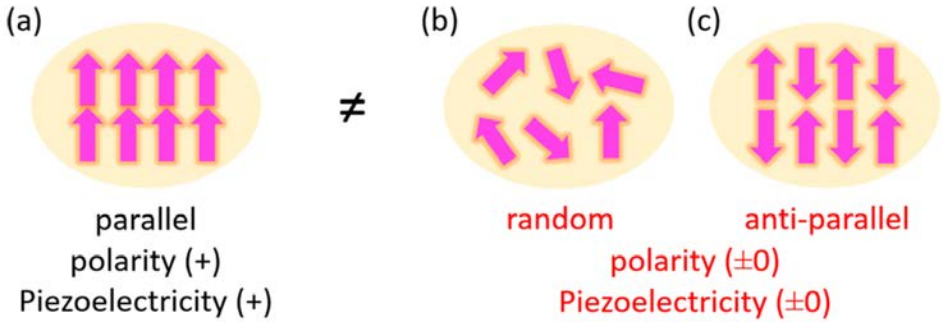

Figure 3. Relationship between polar ordering and net piezoelectricity. The ping arrows represent orientations of individual polar domains. (a) A net piezoelectricity can exist when the polarity is added from parallel arrangements. In the (b) random and (c) anti-parallel arrangements of the polar domains, the polarity as well as piezoelectricity become zero due to symmetric cancellations.[1]

We published the review article reporting these issues in previous literature, covering not only cellulose, but also other biomaterials such as structural proteins.[1] Possible mechanisms, molecular origins and suggestions for a proper investigation of piezoelectricity of the biomaterials are covered. The review article will provide technical guidelines for future studies of piezoelectric composite materials with biologically-derived components.

2. Selective detection of polar domains of cellulose using vibrational SFG spectroscopy

In order to identify the relationship between polarity and piezoelectricity of CNCs, a clear evidence of polar ordering is required. Even though it is one of the most important parameters for investigating piezoelectric properties, the physical evidence of polar ordering has been missing in previous literature. It is mainly because polarization of biomaterials is typically weak and obstacle exists for conventional techniques due to surrounding components. In order to overcome these obstacles, we employed vibrational SFG spectroscopy, and proved its capability of selectively characterizing polar ordering of CNCs.

SFG is a nonlinear optical process, which uses two photons with different frequencies - typically one visible and one IR - and detects the sum frequency of two. The SFG intensity (I_{SFG}) is proportional to the square of second order susceptibility ($\chi^{(2)}$), intensity of visible (I_{VIS}) and IR (I_{IR}).

$$I_{SFG} \propto |\chi^{(2)}|^2 \cdot I_{IR} \cdot I_{VIS} \qquad (1)$$

$$P = \varepsilon 0\,(\chi^{(1)}E + \chi^{(2)}E^2 + \cdots) \qquad (2)$$

The $\chi^{(2)}$ relates the polarization of material (P) and electric field (E) as shown in eq 2. It is a third rank tensor and it is non zero only in non-centrosymmetric media; it is zero for all centrosymmetric or random media. This nature of $\chi^{(2)}$ makes SFG such a strong technique to detect polar domains.

2.1. Probing polarization of piezoelectric P(VDF-TrFE) using SFG

As a proof-of-concept, we first identified the ability of SFG to quantify the polarization of ferroelectric polymer, P(VDF-TrFE). In this study, we proved that the SFG intensity is proportional to the polarization of P(VDF-TrFE) upon poling.[2] All ferroelectric materials are also piezoelectric, and they have a spontaneous electric polarization which can be reversed by applying electric field.[39] In β-phase crystalline P(VDF-TrFE) (all-*trans*), the parallel alignment of PVDF chains adds up polarity of unit cells originated from a strong dipole (-CF_2-), and this makes it ferroelectric.[40] Before poling, the direction of polarization among neighboring domains is random; thus, the P(VDF-TrFE) film does not have a net polarization, piezoelectricity nor SFG signal. Upon poling, the -CF_2- dipoles rotate along the electric field, and it produces non-zero polarization.[41] This also gives rise to the SFG signal as -CH_2- groups are aligned.

Fig. 4d plots the SFG spectra of the PVDF-TrFE film measured *in situ* while the applied electric field varies continuously at 10 mHz rate. Fig. 4c shows the total SFG peak area versus electric field plot (I_{SFG}-E) and the polarization hysteresis (P-E) curve. It can be clearly seen that I_{SFG} is proportional to the square of polarization. This result shows that SFG can quantitatively probe the polar ordering of piezoelectric polymers by tracing the intensity of certain dipole transitions.[2]

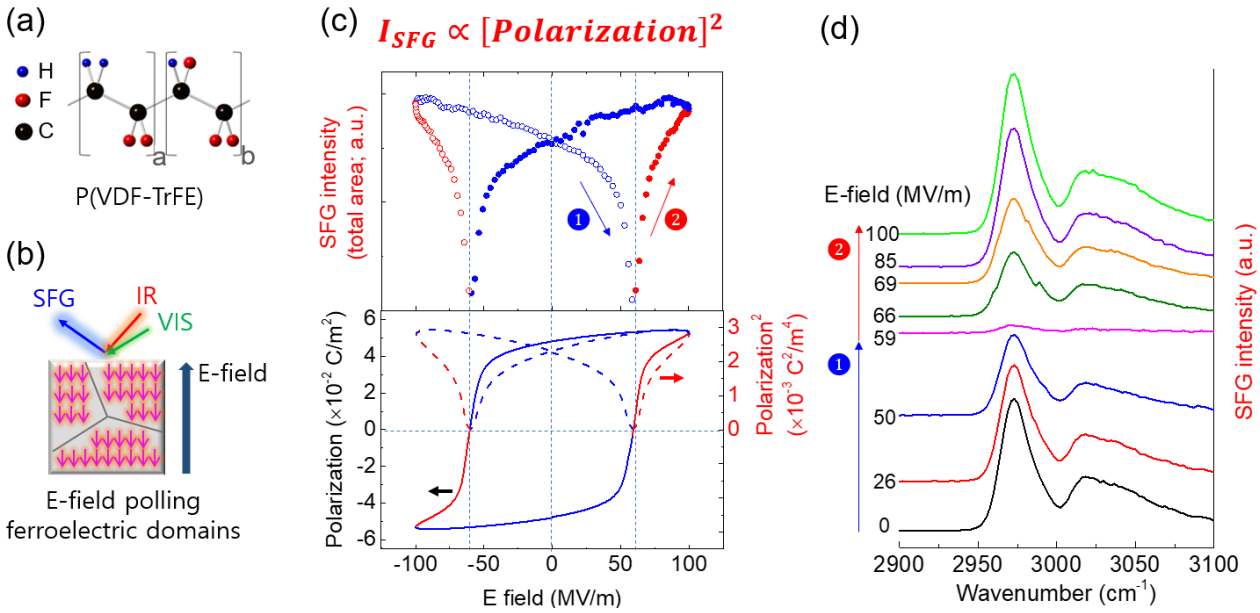

Figure 4. Schematic illustrations of (a) P(VDF-TrFE) repeating units and (b) *in-situ* SFG measurement of the electric field-induced polling process of P(VDF-TrFE). (c) SFG intensity (I_{SFG})–E and polarization (P)–E hysteresis curves obtained during the poling process. (d) SFG spectra measured at selected electric fields. Two peaks at 2973 and 3016 cm^{-1} are assigned to the stretch modes, d^+ and d^- of the CH_2 group, respectively.[2] In I_{SFG}–E plot, I_{SFG} (symbol) is obtained from the total area of both symmetric (d^+, 2973 cm^{-1}) and asymmetric (d^-, 3016 cm^{-1}) SFG signals. In P–E plot, the P^2–E curve is shown for the comparison with I_{SFG}–E curve. The poling and depoling cycles are shown in red and blue colors, respectively.

It is important to note that cellulose has much more complicated structure compared to PVDF. PVDF is a linear straight-chain of (C_2H_2-C_2F_2) monomers and cellulose is a linear chain of β-linked D-glucose with ring-form units ($C_6H_{10}O_5$). In the β-phase PVDF crystals, the strong net dipole is formed from (-CF_2-) aligned along one direction, but in cellulose Iβ crystals, the dipoles of hydroxyl groups are aligned in multiple directions. More importantly, cellulose is not ferroelectric, which means that the orientation of dipoles cannot be switched or reversed by applying electric field.[1] Thus, more systematical approach for the SFG-polar ordering analysis is required for CNCs.

2.2. Characterization of polarity of cellulose using SFG

The polar ordering of cellulose can be identified by analyzing SFG peaks of C-H and O-H stretching modes. Lee et al. obtained the TD-DFT calculations of SFG signal dependence on parallel versus anti-parallel cellulose packing as shown in Fig. 5.[42] Fig. 5a shows the schematic of truncated cellulose Iβ dimeric units used in the TD-DFT calculations. Glucose dimers represent a single crystalline domain, and two crystallites were stacked along a-axis for the parallel case. For the anti-parallel case, one of the two crystallites is rotated around the Z-axis as shown in Fig. 5b. The simulated SFG spectrum for the parallel case shows that the O-H peaks are much stronger than the C-H peaks as shown in Fig. 5c. On the other hand, the anti-parallel case shows that the overall SFG intensity is much smaller than the parallel case, and the C-H peaks are stronger than the O-H peaks as shown in Fig. 5d. These differences are attributed to the symmetry cancellation of O-H vibrational modes within the SFG coherence length. The dipole transitions of the O-H group are much more sensitive to the polarity of cellulose compared with the C-H groups. In the anti-parallel case, the O-H dipoles point the opposite directions between two neighboring chains such that $\chi^{(2)}$ of O-H components are substantially cancelled within the coherence length. The experimental SFG measurement accords with the simulated results as the cellulose Iβ (parallel chain packing) appears much higher O-H/C-H peak ratios than cellulose II (anti-parallel packing).[43]

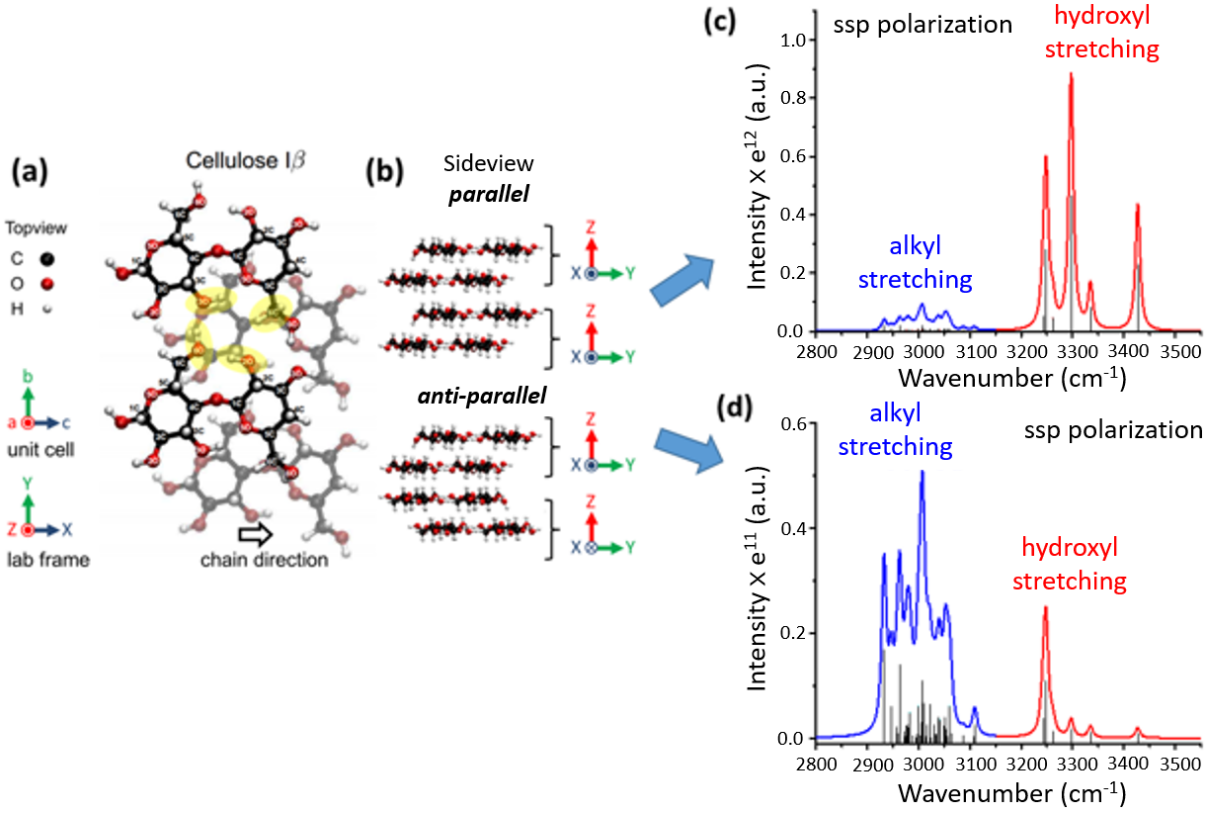

Figure 5. Computational models and simulated SFG spectra of cellulose Iβ achieved by TD-DFT calculations. (a) Top view of the single crystalline domain modeled with truncated dimers (b) Side-view of the two domains stacked in parallel and anti-parallel manner. Simulated SFG spectra at the *ssp* polarization combination (*s*-polarized SFG, *s*-polarized 800 nm laser, *p*-polarized IR) for crystallites packed in (c) parallel and (d) anti-parallel manner, respectively. In the laboratory frame, the laser incident plane lies in the XZ plane; the *p*-polarization has electric fields in the X and Z directions, while the *s*-polarization has an electric field in the Y direction which is parallel to the b-axis.[42]

2.3. Investigation of polar ordering and dielectric properties of EAPap

EAPap, which was invented by Jaehwan Kim's group, has been reported to have strong electromechanical responses in the literature.[14, 16, 44-45] Among cellulose-based materials, the reported piezoelectric coefficients of EAPap have been the highest in the previous literature.[18] In this project, we investigated the polarity and dielectric properties of EAPap in order to the address its origin of such a strong electromechanical responses.

EAPap is composed of cellulose II crystallites, which have the anti-parallel arrangement of cellulose chains.[14, 16, 44-46] As we discussed, due to the anti-parallel arrangement in the cellulose II crysatl,[43] the piezoelectricity and polarity should be very small or almost zero. Fig. 6a shows the evidence of negligible net polarity from hydroxyl (O-H) groups in the anti-parallel arrangement of cellulose chains in EAPap. The arrangement of hydroxyl groups is actually very important to explain piezoelectricity because they are the most probable origin of piezoelectricity of cellulose.[47] The SFG spectrum of Avicel with cellulose Iβ crystals (parallel arrangement) is included for the comparison. In cellulose Iβ crystals, the chains are arranged in parallel such that the SFG signal from hydroxyl groups (3200 – 3500 cm^{-1}) is almost comparable to the signal from CH/CH_2 groups (2800 – 3000 cm^{-1}). On the other hand, the SFG signal from hydroxyl groups of EAPap is zero (below the noise level of the background) because they are aligned in anti-parallel fashion within the SFG coherence length. This SFG result shows that there is no net polar ordering from hydroxyl groups in both cellulose II crystals and non-crystalline domains of EAPap. Given the anti-parallel arrangement of domains, the piezoelectricity should be reduced, and thus we expect that the piezoelectricity of EAPap is extremely small, if not zero.

Fig. 6b shows the dielectric loss as a function of frequency. Although the behavior of the dielectric loss at higher frequencies is typical, at the lower frequencies (f < 1 Hz), there is a marked increase in the loss, which shows a clear dependence on f^{-1}, indicating ionic conduction. EAPap samples still have residual ions even after rigorous rinsing and drying processes. Even small quantities of ionic residues in EAPap can generate a large deformation under electric field because of ion migration, and it could have a

large contribution in the converse piezoelectric measurements. The presence of ions can also affect the direct piezoelectric measurement as mechanical bending can induce migration of ions from the compressed regions to expanded regions.[48] Therefore, without ruling out the response of ions in EAPap, the observed electromechanical coupling effects cannot be attributed to piezoelectricity.

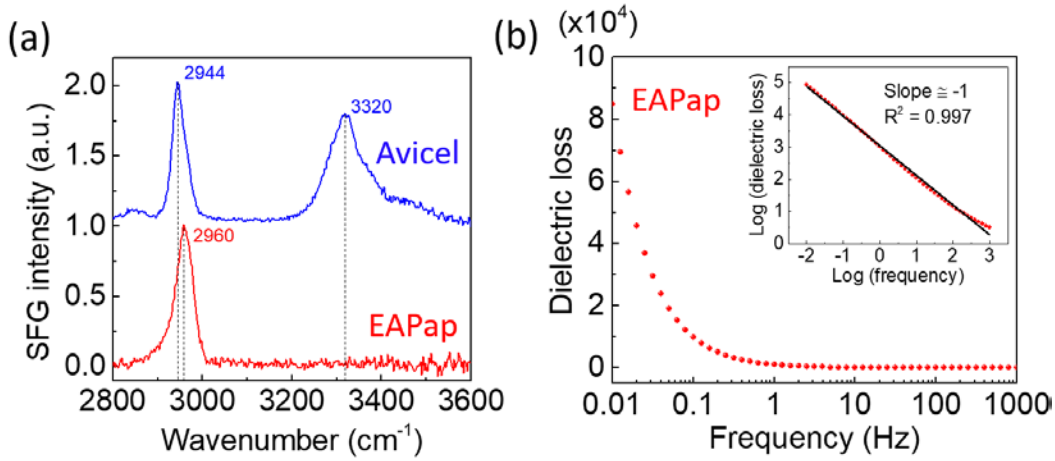

Figure 6. (a) Normalized *spp*-SFG spectrum of Avicel (cellulose Iβ) and EAPap (cellulose II + non-crystalline cellulose). (b) Dielectric loss of EAPap as a function of frequency. The same data in log scale with the linear fitting is included as the inset.

Reviewing previous literatures and investigating the most well-known piezoelectric composite (EAPap), we concluded that the piezoelectric values in the literature should be not solely from true piezoelectricity, but mostly from other intrinsic and extrinsic electromechanical couplings. In order to investigate further, whether structural orderings can induce the polar ordering of CNCs, we first tested the dispersion of CNCs in organic solvents and polymer matrix (section 3), and then identified their translational and rotational behaviors under external fields/forces (section 4).

3. Dispersion of individual CNCs in an organic solvent and polymer matrix

It is important to disperse individual CNCs in an organic solvent to test electric-field induced polar ordering as well as make a uniform CNC-polymer composite. Aggregated CNCs disturb a control of their polar ordering under external field/force and make characterization steps very difficult. In order to resolve the aggregation issue, we tested the dispersion of CNCs in polar and non-polar organic solvents.

The dynamic light scattering (DLS) results show that CNCs are aggregated in non-polar organic solvents such as THF and toluene (Fig. 7a). On the other hand, CNCs are well-dispersed in water and polar organic solvents such as DMF, ethanol and NMF; this was supported by the fact that the

hydrodynamic particle size of individual CNCs does not change significantly in these solvents (hydrodynamic diameter peaks of 40-80 nm). In pure ethanol, CNCs were measured to have a bit bigger size distribution (peak at 80 nm); however, we confirmed that most crystals are individually dispersed, from atomic force microscopy (AFM) images of the CNCs deposited on a solid substrate. With a small amount of the water content (5 wt%), most of the CNCs are also individually dispersed in DMF. It is also confirmed that CNCs are dispersed well in NMF. The main reason for this difference in particle size distributions of CNCs in polar and non-polar organic solvents is due to the lack of electrostatic repulsion between CNCs in non-polar solvents.

Additionally, we attempted the coating of cationic dimethyldioctadecylammonium bromide (DODA) and sorbitan monostearate (SorM) surfactants on CNCs to evaluate how the adsorbed surfactants can assist the dispersion of CNCs in non-polar solvents. Fig. 7b and Fig. 7c show the results of particle size analysis after coating the surfactants on CNCs in water (polar) and toluene (non-polar). For the case of SorM coated CNCs in water, huge aggregations occurred that we could not even measure the size of particles with the DLS technique. As shown in Fig. 7b, coating the cationic surfactant (DODA) onto CNCs causes partial aggregation at a low concentration (0.001 wt%) of DODA, and severe aggregation at a higher concentration (0.003 wt%) of DODA. Also, coating DODA and non-ionic surfactant (SorM) on CNCs in toluene causes the aggregation of CNCs as shown in Fig 7c. Heux et al reported a good dispersion of CNCs in non-polar solvents by coating with certain surfactants[49-50]; however, they showed only optical images and turbidity of the solutions, which just provide an evidence of macroscopic dispersions of CNCs. Through these tests, we concluded that cationic and non-ionic surfactants can make CNCs still aggregate in water and toluene.

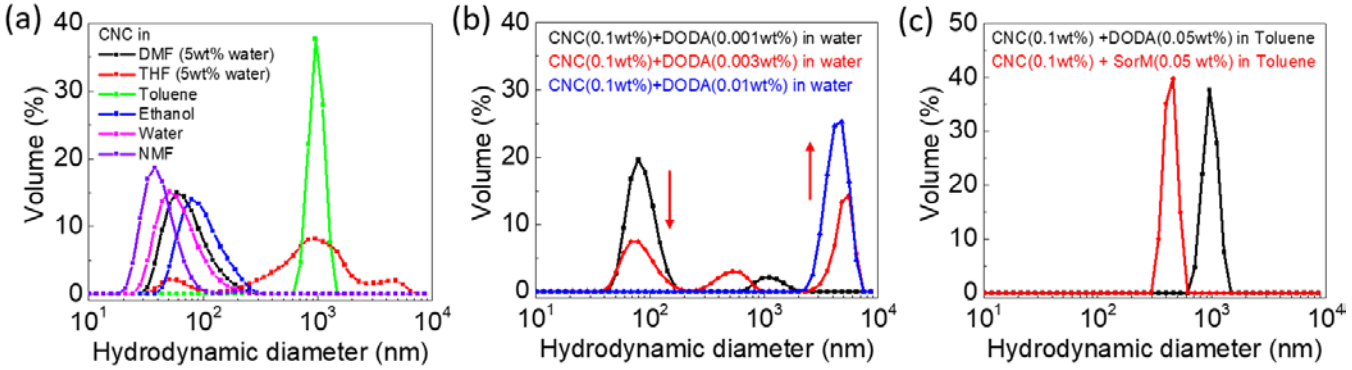

Figure 7. Particle size analysis of CNCs in various solvents by using DLS. (a) Hydrodynamic diameter of bare CNCs in water, polar organic solvents (DMF, ethanol, NMF) and non-polar organic solvents (THF, toluene). (b) CNCs with various concentrations of DODA in water. (c) CNCs coated with DODA and SorM in toluene.

After the solvent exchange from water to DMF+PVAC followed by evaporation of DMF and curing PVAC, we successfully processed a composite in which isolated CNCs are embedded in the PVAC matrix as shown in Fig. 8. There are other polymers commercially available which can be dissolved in polar organic solvents such as polyurethane and polyacrylonitrile. Through the solvent exchange and curing process, individual CNCs would be embedded in such polymers, too. Aligned CNCs inside a fluidic state can be fixed by solidifying the polymer matrix. The main challenge here is to find optimal conditions of external forces to align CNCs in parallel in a liquid medium.

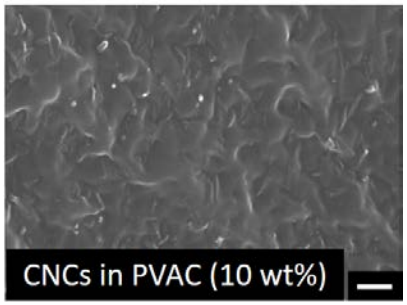

Figure 8. Scanning electron microscopy (SEM) image of embedded CNCs in PVAC. The scale bar is 100 nm.

4. Understanding translational and rotational behaviors of CNCs under external fields/forces

4.1. Translational and rotational behavior of CNCs under electric field

CNCs have a net dipole and anisotropic polarizability that they have been expected to be aligned along the applied electric field.[11, 51-53] We tested the efficacy of the electric field-induced alignments of CNCs using the method which was introduced earlier by Csoka et al as shown in Fig. 9a.[11, 51] The bottom fused quartz is coated with a cationic polyethylenimine in order to deposit negatively charged CNCs. To avoid electrolysis on the electrodes, ethanol was used as a liquid medium instead of water. A small drop of the ethanol solution containing CNCs is placed between a tilted glass slide and a fused quartz with coated electrodes. The tilted glass slide is dragged at a constant speed while the electric field is applied. This method deposits CNCs between the electrodes as a thin layer (around 50 nm). The orientation of CNCs under electric field is expected to be fixed as the solvent evaporates.

Under an AC electric field, locally aligned but inhomogeneous patches of CNCs appeared as shown in Fig. 9b. Some regions showed the aligned CNCs along the AC field, but other regions showed the aligned CNCs along the glass sliding direction (perpendicular to the electric field). A dragging force

from the glass sliding could align the long axis of CNCs along the sliding axis. It was reported in literature that cellulose Iβ crystals have a strong polarizability that they can be aligned along the AC electric field.[51] The rotational torque from glass sliding (mechanical) and AC electric field (electrical) are acting on CNCs at the same time, and locally different orientations of CNCs are appeared. Habibi et al theoretically calculated the optimal AC field condition to align CNCs, and showed experimental results of aligned CNCs along the field.[52, 54] Csoka et al reported the increased piezoelectric properties of CNCs aligned under AC fields.[11] However, they did not provide any evidence of polar ordering in prepared samples, which makes it difficult to believe that the applied AC field indeed induces the parallel alignment (one direction) of CNCs. With only AFM or SEM images, it is not possible or conclusive to tell if the aligned CNCs are parallel or anti-parallel since they have a symmetric appearance. Under DC electric field (50% duration pulse), negatively charged CNCs are mostly moved toward the positive electrode as shown in Fig. 9c. Other conditions of DC field: 5 V/250 μm at 1 MHz, 10 V/250 μm at 100 Hz were tried, and they also showed the translation of CNCs toward the positive electrode. These results show that the electrophoretic translation is much more dominant over the electric rotation of CNCs.

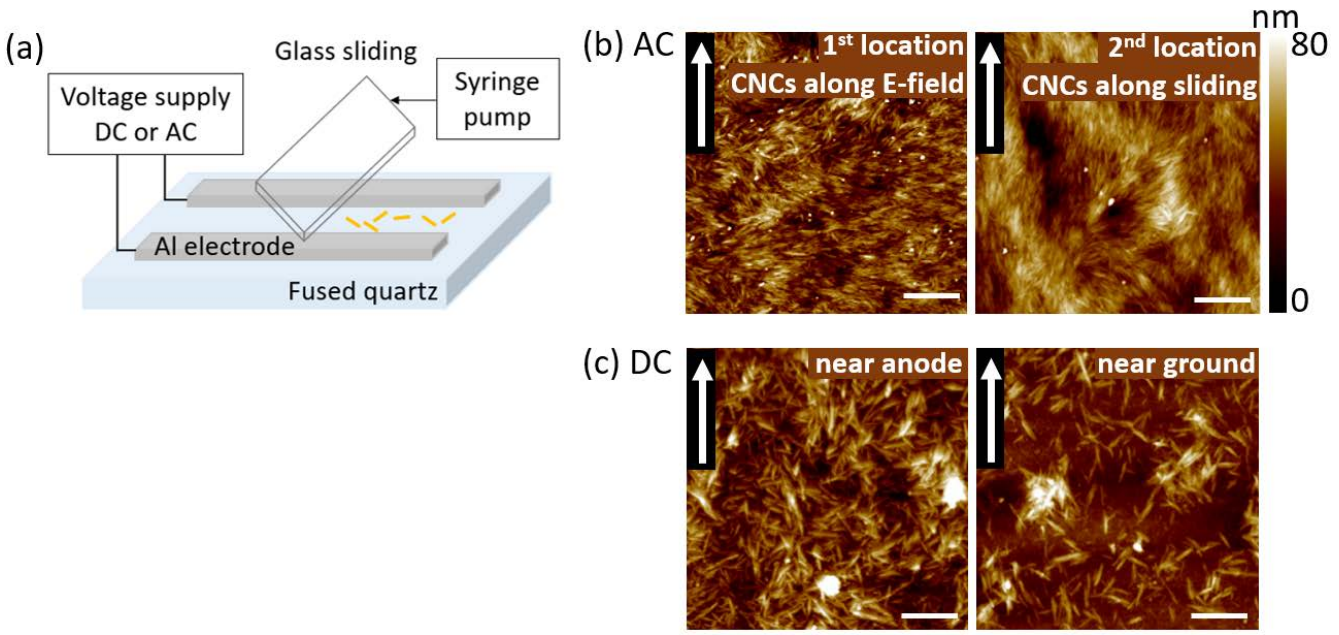

Figure 9. (a) The glass sliding method for testing AC and DC electric field induced alignments of CNCs. CNCs in ethanol (1wt%) is dropped on the fused quartz with coated Al electrodes. The flat glass is dragged along the long axis of electrodes at a constant rate while AC or DC electric field is applied. (b) AFM images of locally aligned CNCs along the applied AC (20 V/500 μm, 2 kHz) electric field and along the glass sliding axis. (c) AFM images of CNCs around 20 μm from the positive and ground electrodes after DC pulse (+10 V/250 μm, 10 Hz, 50% duration) is applied. White arrows in (b) and (c) represent the direction of glass sliding. The white scale bars are 1 μm.

In order to test the polar ordering of CNCs under a DC electric field, electrophoretic deposition (EPD) method was employed as shown in Fig 10a. In this method, a DC electric field is applied on CNCs in DMF using two electrodes, which translate negatively-charged CNCs onto the positive electrode. Fig. 10b shows the cross-polarized microscopy (CPLM) images of CNCs deposited on the ITO electrode at various DC field conditions. Without applying the DC field, no birefringence appeared. Increasing the field magnitude and time, clear birefringence appeared, which originates from the lateral packing (Fig. 10c) of CNCs. The translated CNCs under DC filed are laterally packed on the positive electrode due to the high aspect ratio (~19) of CNCs. We initially expected that EPD-CNC films have some degree of parallel alignment along the short axes of CNCs due to their net dipole moment; however, the SFG investigation showed that the laterally packed CNCs have an anti-parallel arrangement in overall (Fig. 10d). The SFG ratio of OH/CH of the EPD-CNC is much less than that of the randomly arranged CNCs. This means that the polarity of hydroxyl groups in the EPD-CNC is much less than the randomly arranged case because the CNCs are arranged in anti-parallel manner.

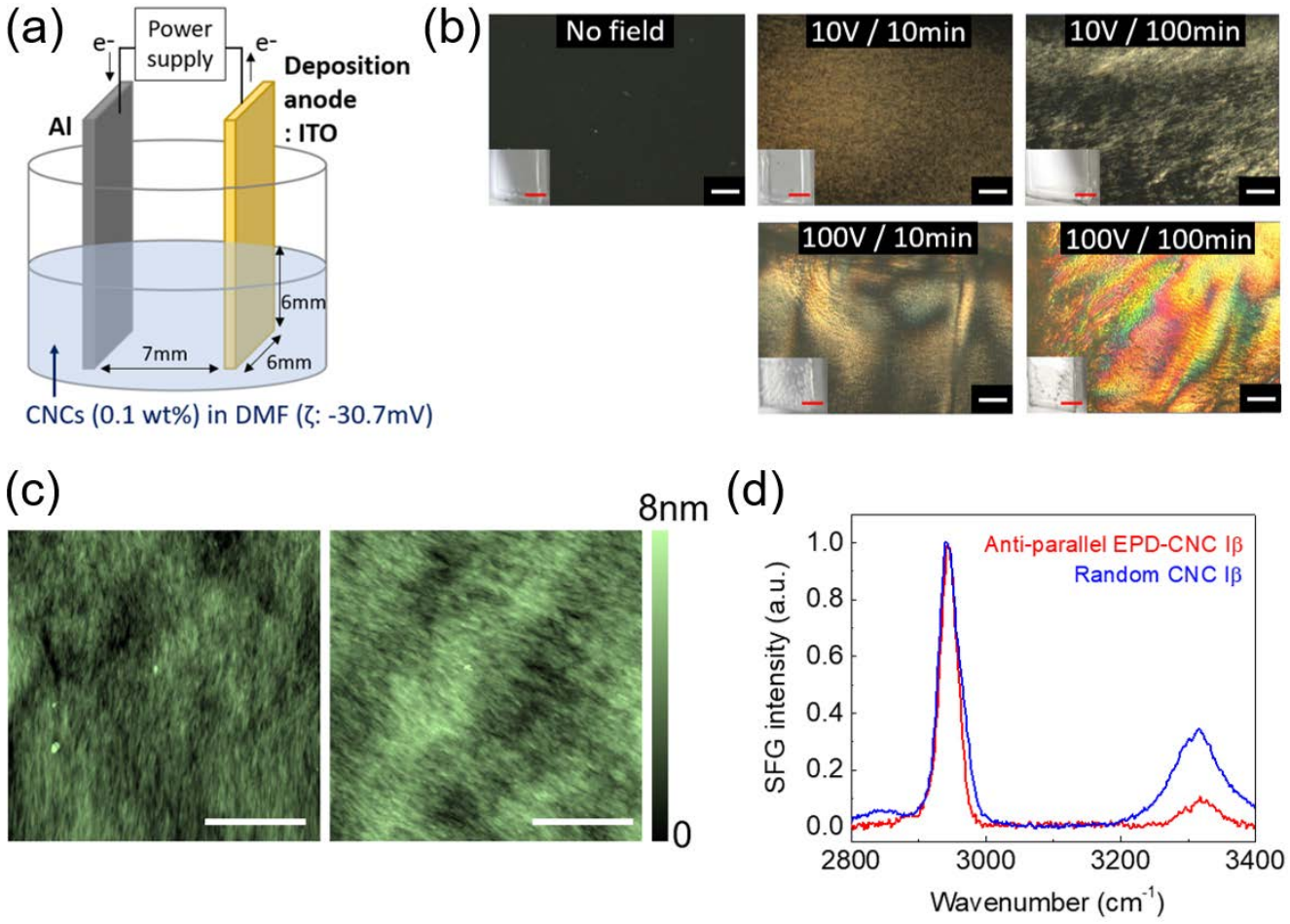

Figure 10. (a) Schematics of EPD for CNCs under DC electric field. (b) CPLM images of the EPD-CNC films on ITO substrates under the given DC electric field conditions. The white scale bars are 50 μm. Non-polarized optical images are included as insets on the bottom left. The red scale bars are 3 mm. (c) AFM images of the EPD-CNC film in two different locations. The white scale bars are 1 μm. (d) SFG spectrum of EPD-CNC Iβ film with the anti-parallel packing and randomly oriented CNC Iβ pellet.[55]

The investigation of translational and rotational behaviors of CNCs under electric field concludes that the effect of surface charge is dominant over the effect of net dipole in a liquid medium where CNCs can freely rotate. Therefore, it is critical to decrease the surface effect in order to see the polar ordering. The electrophoretic translation can be induced by the surface charge whereas the electric rotation can be induced by the permanent dipole moment. CNCs have a negative surface charge (zeta potential: -52 mV) from the sulfuric acid-hydrolysis reactions. This surface charge induces the electrophoretic translation under DC field.[56] The surface charge is actually required to maintain a good dispersion stability in a liquid media; otherwise, they would aggregate. There is an alternative hydrolysis process which uses HCl, instead of H_2SO_4; but, CNCs extracted in this method have very poor dispersion stability and they aggregate easily that further processing becomes very difficult. Bruno et al reported that CNC Iβ, which was used in our study, has a strong permanent dipole moment with which CNCs can rotate under electric field.[53] However, our investigation proved that the rotational torque of the dipole of CNC bulk under electric field is much smaller than the electrophoretic translational force due to the surface charge.

4.2. Chiral nematic phase formation of CNCs under magnetic field

We investigated the chiral nematic order of CNCs in DI H_2O and a polar organic solvent, n-methylformamide (NMF), with and without a H field (0.7 T). The effects of CNC content, solvent, and H-field application were monitored, in situ, with small angle x-ray scattering (SAXS). Three contents were prepared in DI H_2O and, NMF: 6, 8 and 10 wt%. For the solvent exchange, a 100 g of 10 wt% CNC-H_2O solution was diluted by adding 100 g NMF. The CNCs were then dispersed in the diluted solution using high power sonication. The water was removed by distillation at 50 °C at reduced pressure, 50 mbar, using a rotary evaporator. This procedure is used to ensure good dispersion of the CNC in the solvent at all times and avoid agglomerations that can happen when centrifuging is used for solvent exchange. The CNC content in the final solution in NMF was measured by drying small aliquots and measuring the weights before and after drying. The average of the CNC-NMF contents ranged from 9.4 to 9.8 wt%, indicating that traces of H_2O remained in the solution. For the sake of simplicity, the resulting solutions

of the solvent exchange experiment will be referred to as 10 wt% CNC-NMF. SAXS data were collected using a XENOCS Xeuss 2.0 with a Cu Kα source (wavelength λ=1.54189 Å) with high-resolution collimation. Prior to all runs, AgB samples were used to calibrate the sample-detector distance. Prior to the SAXS runs, the CNC suspensions were sonicated and then injected into 1.5 mm capillary tubes. Epoxy was used to seal the tubes to avoid evaporation while under vacuum in the chamber. For measurements without magnetic field, three samples were placed in a multi-sample holder at a 2.5m distance from the detector. For measurements under magnetic field, a setup was built using two NdFeB N52 1 inch-diameter permanent magnets separated at a constant distance of 4 mm, generating a 0.7 T magnetic field. The capillary tube was placed at the center of the gap to be subjected to the strongest generated magnetic field. Fig 11. shows a schematic of the in-situ SAXS measurement under magnetic field.

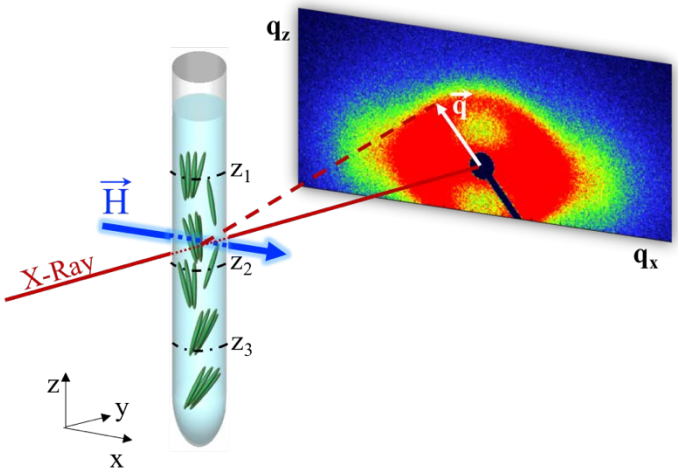

Figure 11. Schematic of the in-situ SAXS measurement under magnetic field: CNC suspensions loaded into a capillary (// z-axis) centered between permanent magnets. The X-ray beam (// y-axis) probes orthogonal to the magnetic field direction (// x-axis). Anisotropic scattering is collected on an area detector on xz-plane.

In the chiral nematic phase, the 2D scattering of CNCs takes an oval shape with the long axis close to the horizontal direction, indicating that the CNCs are aligned mainly along the vertical direction, parallel to the capillary tube length axis. This indicates that the overall direction of the CNCs is imposed by the geometrical constraints imposed by the capillary tube on the CNC rods in suspension.[57-58] When the magnetic field is applied, the CNCs tend to align with their long axis perpendicular to the magnetic field due to their negative diamagnetic anisotropyz.[59] In this work, the magnetic field is applied perpendicular to the capillary tube, as shown in Fig. 11. Thus, it is expected that the magnetic field will further enhance the alignment of the CNC long axis parallel to the capillary length. The CNC ordering

was assessed by the anisotropic order parameter (S) computed by fitting the azimuthal profile I(χ) at q_0, where q_0 is the scattering variable for the first peak in Kratky plot, which corresponds to the interparticle distance. Following the procedure detailed in the literature[59], the azimuthal intensity at q_0, is fitted to Eq (3), *C* is a scaling constant, χ is the angle that varies from 0 to $\pi/2$, χ_0 is the alignment direction, and η is an ad hoc order parameter that varies from 0 (fully isotropic) and 1 (fully anisotropic).

$$I(\chi) = \frac{C(1-\eta^2)}{(1+\eta)^2 - 4\eta cos^2(\chi - \chi_0)} \qquad (3)$$

And if the orientation distribution is known, the orientation order parameter S is computed using Eq (4):

$$S = \frac{\int_0^{\pi/2} f(\chi') \frac{3cos^3\chi' - 1}{2} sin\chi' d\chi'}{\int_0^{\pi/2} f(\chi') sin\chi' d\chi'} \qquad (4)$$

where $f(\chi)$ is the orientation distribution, the function I(χ) listed in Eq (3), is a good representation of the orientation distribution. The substitution $\chi' = \pi/2 - \chi$ is required because χ is defined with respect to q_z axis, while χ' is defined with respect to the q_x axis. Following this definition, an isotropic distribution would lead to S=0, while a perfect alignment parallel to the director would have S=1. Using the same definition, S=-0.5 for a perfect antialignment, where all the CNC rods are perpendicular to the director, but they have different orientations within the plane orthogonal to the director. Fig. 12 shows examples of 2D scattering intensity and the corresponding azimuthal profiles with fitting curves. The 2D scatterings and the azithumul profiles reveal a more well-defined anisotropy in H_2O (S = -0.49) than in NMF (S = -0.20).

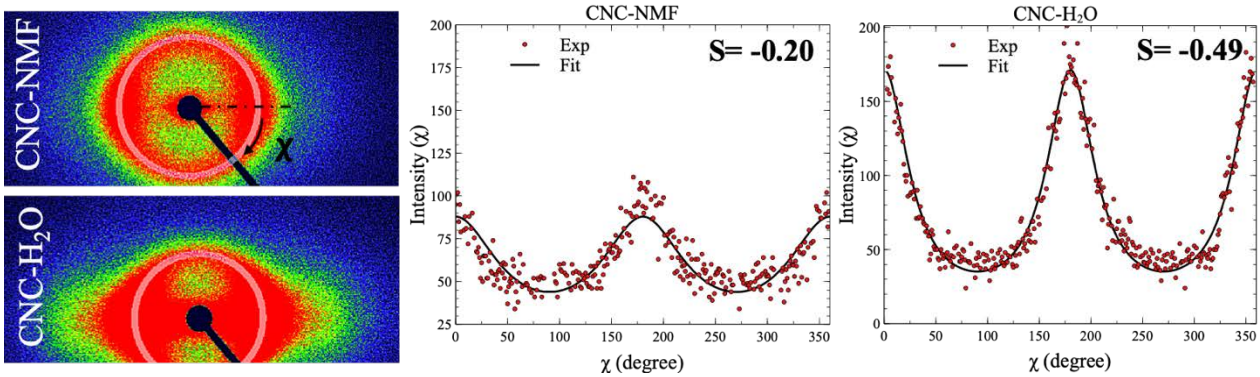

Figure 12. 2D SAXS scattering intensity under magnetic field and the azithumul profiles at q_0 with fitting curves of 6wt% CNC-NMF and 6wt% CNC-H_2O.

Fig. 13 shows the anisotropic order parameter (S) computed from the final sets of data collected for all CNCs suspensions, with and without magnetic field. Overall, the CNC-H_2O suspensions show

higher degrees of anisotropic alignment (larger absolute values in S) than the CNC-NMF suspensions. In the absence of the magnetic field, the magnitude of S for the CNC-H_2O suspensions increases slightly from 0.15 to 0.19 as the CNCs content increased from 6 to 8 wt% loading, then plateaus with 10 wt% CNC loading. With NMF as the solvent, the magnitude of S increases from 0.03 to 0.13 when the CNCs content increases from 6 to 8 wt%, then it decreases to 0.02 at 10 wt% CNC loading. The application of the magnetic field (0.7 T) significantly enhances the degree of anisotropic alignment. In H_2O suspensions, the magnitude of S is the highest (0.497) with 6 wt% CNC loading. The order parameter then decreases to 0.42 and 0.27 at 8 and 10 wt%, respectively. With NMF as the solvent, the order parameter has the same non-monotonic trend observed without magnetic field. The maximum order is achieved at 8 wt% CNC content (S = -0.26).

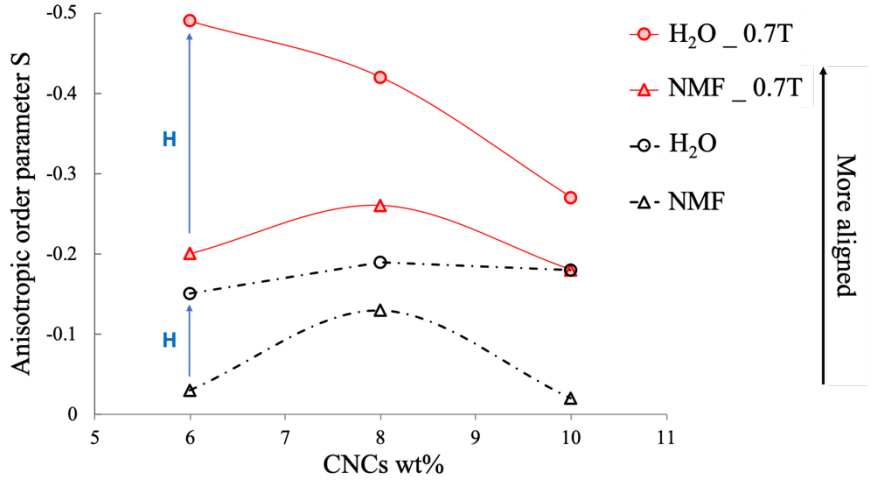

Figure 13. Computed anisotropic order parameter S from the final sets of measurements (after ~20hrs), with and without magnetic field for all the chiral nematic phases of the CNCs suspensions.

The CNCs chiral nematic contents in both solvents with the highest order achieved, 6.7 and 8 wt% in H_2O and NMF, respectively, were selected to be further investigated by transferring the order from the liquid to the solid state by evaporating the solvent under a strong magnetic field, 4 T. The suspensions were first sonicated, using a higher power sonication at 40% power, to disperse the CNCs. Control samples were prepared by pouring the solutions in petri dishes, left at room temperature for 2 hours, then placed in oven at 50°C for 16 hours. Films made with NMF required another 6 hours at 60 °C to dry. The films dried under magnetic field were prepared as follows: Keep samples under 4 T for 2 hours at room temperature, then apply 50 °C temperature while the magnetic field is kept on for 18 hours. All the samples, control and H-dried, were placed under vacuum at 60 °C for 10 hours to remove any residual solvent.

Fig. 14 shows scanning electron microscopy (SEM) images of the films cross-sections where an enhancement of the CNCs alignment in films dried under magnetic field is visually confirmed. The SEMs of control samples show some planar order as the CNCs formed layers of chiral nematic tactoids. The planar configuration of the CNCs in the dried film is influenced by the geometrical constraints presented by the sample dimensions, where the thickness is much smaller than its width and length, and the fact that it was decreasing gradually as the solvent slowly evaporated.[60] The 2-hour holding at room temperature before drying the samples allowed the CNCs to self-assembly into an anisotropic phase. And the slow drying at the relatively low temperature, 50 °C, kept the CNCs self-assembly stable as the solvent gradually evaporated. The samples dried under 4 T have better defined layers as can be seen in Fig. 14, indicating that the magnetic field enhanced the packing of CNCs, compared to the control samples.

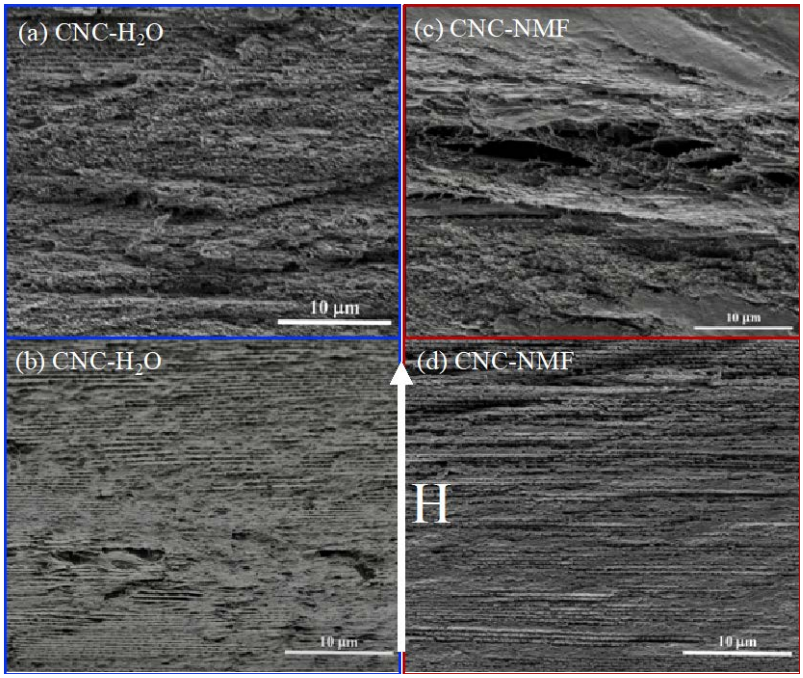

Figure 14. (a) SEM images and (b) *sps*-SFG spectrum of dried CNC films from NMF with and without 4T applied during the drying process.

The type of the CNC order, parallel vs. antiparallel, was investigated using SFG, which is a strong tool to investigate the polar ordering.[2] A previous study established that the OH/CH ratio of the signal collected by SFG can be used to distinguish between parallel and anti-parallel packing of CNCs. CH vibrational modes are mostly normal to the cellulose sheet, whereas OH vibrational modes are mostly within the cellulose sheets. Thus, OH vibrational modes are more sensitive to the parallel and antiparallel

packing of CNCs. When the CNCs are arranged in an anti-parallel packing, the OH vibrations contribution to the SFG signal would cancel out.[61] In the SFG measurements, cross-section of the dried CNCs films were placed on the sample stage in a way that IR polarization (*s*) is perpendicular to the applied 4 T as shown in the schematic in Fig. 15a. The collected SFG spectra were normalized with respect to the peak at 2944 cm^{-1}, which is attributed to CH_2 asymmetric stretching mode of CNC, and they are shown in Fig. 15(c) and (d). The peak between 3250–3400 cm^{-1}, which corresponds to the OH/CH peak ratio, decreased in the 4 T-dried samples compared to the control samples. Fig. 15b shows a comparison of the integrated-intensity ratios of OH/CH stretching modes between the control and 4 T-dried samples. The decrease in the OH/CH ratio in the aligned samples indicates a strong antiparallel packing of the CNCs when dried under the magnetic field. The 4 T magnetic field orders the chiral nematic tactoids that form due to the CNCs self-assembly in the samples at a local level, to achieve a global order in the resulting dried film.

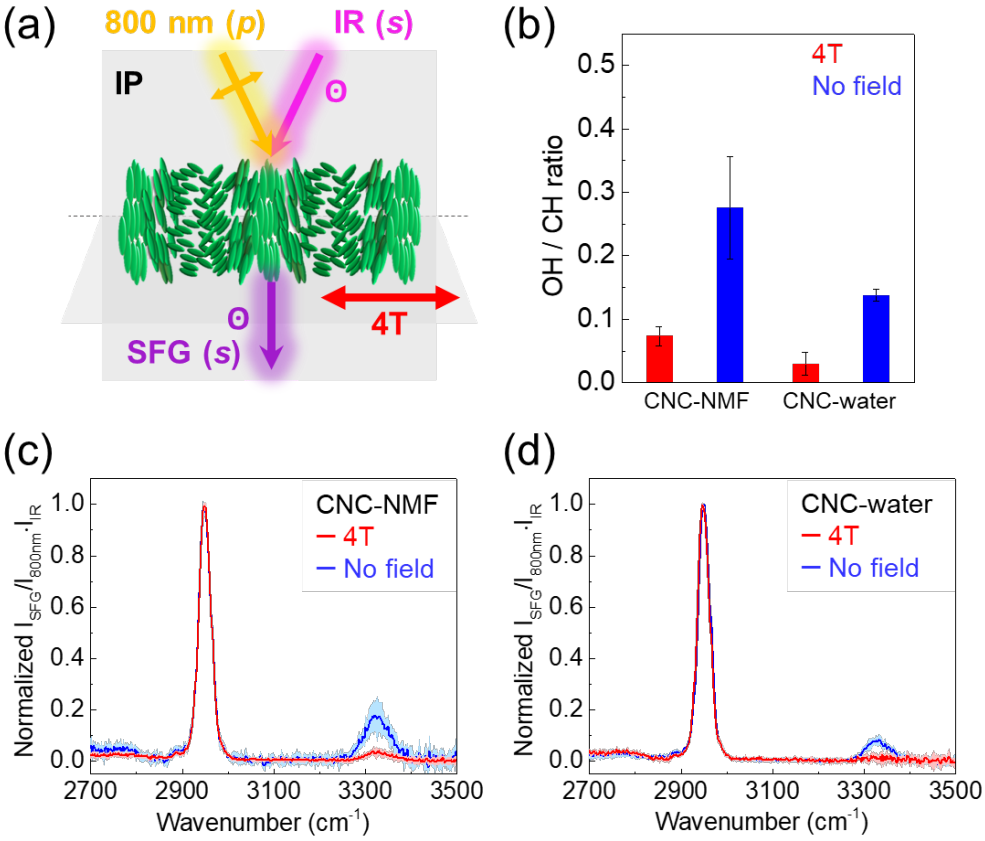

Figure 15. (a) Schematics of SFG (sps, s-polarized SFG, p-polarized 800 nm, s-polarized IR) spectroscopic measurement on the chiral nematic CNC Iβ films in a transmission mode. Total 4 CNC Iβ films were measured: evaporated NMF with and without magnetic field (4T), and evaporated water with and without magnetic field (4T). The films were placed as applied 4T during the evaporation of solvents

is along the incidence plane (IP) and the SFG sample stage. (b) The integrated-intensity ratio of OH (3250-3400 cm^{-1}) over CH (2850-3000 cm^{-1}) and (c, d) full SFG spectrum of 4 different CNC Iβ films. The SFG signals are averaged from 5-8 different locations (standard deviations with sky blue and pink bands) on each film. The intensity of SFG (I_{SFG}) is divided by the intensity of 800 nm (I_{800nm}) and IR (I_{IR}) beams, and then normalized by the signal at 2944 cm^{-1}

4.3. Nematic phase (anti-parallel) formation of CNCs at the air/water interface

It is proven that structural ordering does not necessarily induce the polar ordering of CNCs in this study. Compression-induced lateral packing of CNCs at the air/water interface was made using LB method, and their polar ordering analysis was performed using *in-situ* SFG as shown in Fig. 16a. Since extracted CNCs through a sulfuric acid hydrolysis has a negative surface charge on their surfaces, they are well-dispersed in water. Cationic surfactants like DODA are necessary to attract CNCs to the air/water interface.[62-63] The deposited CNCs on a fused quartz substrate showed 8-9 nm thickness, which proves a monolayer formation of CNCs at the interface. Fig. 16d shows the deposited DODA/CNC on the fused quartz substrates at different surface pressures (SPs). In the expanded region, randomly oriented CNCs are appeared inhomogeneously on the substrate. Compressions to 1mN/m and 10 mN/m make them more uniformly covered on the substrates, but still randomly arranged. Further compressions to 30-50 mN/m laterally pack CNCs.[4]

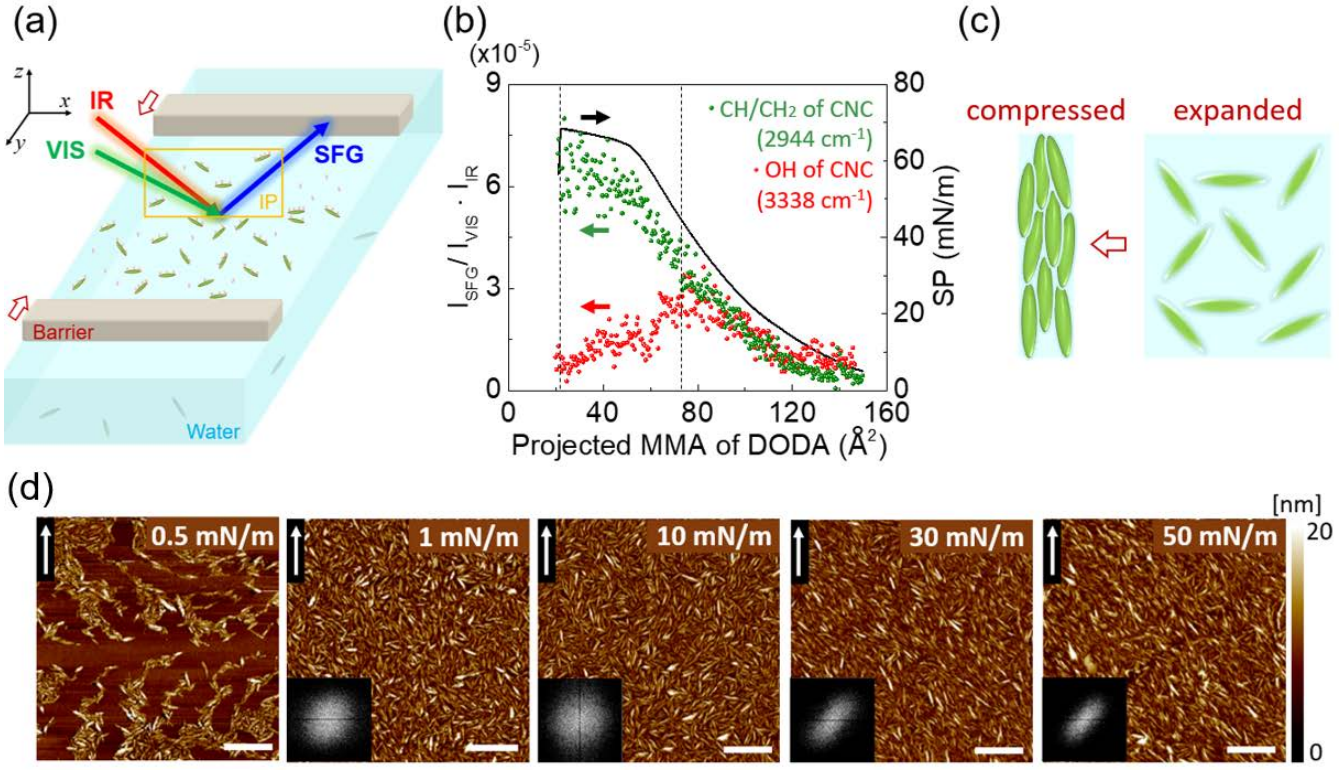

Figure 16. (a) Schematic illustration of the *in-situ psp*-SFG measurement of CNC and DODA at the air/water interface. Laser beams of 532 nm (VIS) and tunable infrared (IR) are overlapped on the sample surface and the photon whose energy is the sum of two input photons (SFG) is detected. (b) Compression isotherm profile (black line; right axis) and normalized SFG intensity ($I_{SFG}/ I_{VIS} \cdot I_{IR}$; left axis) of the CH/CH_2 peak of CNC at 2944 cm^{-1} (green) and the OH peak of CNC at 3338 cm^{-1} (red) as a function of projected MMA of DODA. (c) Schematic illustration of CNC packings at the expanded and compressed states (top view, xy-plane). (d) AFM images of the CNCs deposited at gaseous phase (0.5 mN/m), liquid phase (1, 10 mN/m) and solid phase (30, 50 mN/m). 2D-fast Fourier transform (FFT) of CNCs were included as insets. The arrows represent pulling directions of the fused quartz substrates from LB trough for the deposition. The white scale bars are 1 μm.[4]

Through the *in-situ psp*-SFG measurement on the DODA/CNC at air/water interface, polar ordering of CNCs was selectively monitored as shown in Fig. 16b; the *psp*-SFG measurement is sensitivity to only chiral species.[64] SFG intensities at two specific wavenumbers (3338 cm^{-1} for OH stretching mode and 2944 cm^{-1} for CH/CH_2 stretching mode) were measured. While the CH/CH_2 peak increases monotonically during the compression, the OH peak at 3338 cm^{-1} is increased until the SP reaches 40 mN/m, and then decreased by further compression.[4] In our previous SFG investigations, when CNCs are uniaxially packed with statistically equal probabilities toward opposite directions, the OH modes increases, and then decreases as the inter-particle distance from the value larger than SFG coherence length (30-40 nm in this case) to the value smaller than the coherence length.[42,65] This is mainly due to the symmetry cancellation of SFG signal from OH stretching modes between neighboring CNCs in the anti-parallel arrangement.[42] This symmetry cancellation effect does not appear for the CH/CH_2 modes because there is a rotational freedom during the compression. This result shows that lateral packing of CNCs can be made under compression, but it cannot induce the polar ordering of CNCs.

4.4. Anti-parallel alignment of CNCs in a polymer matrix under mechanical stretching

In this study, we proved that a mechanical stretching also induces the anti-parallel alignment of CNCs, which would decrease the net piezoelectric properties. Extracted Iβ CNCs were embedded in polyacrylonitrile (PAN) matrix as 20wt%, and mechanically stretched by gel spinning.[66] The samples were prepared in Prof. Satish Kumar's group at Georgia Tech. Fig. 17a shows the schematic illustration. Anti-parallel alignment of CNCs should be entropically more favorable than parallel alignment by mechanical stretching of randomly oriented sample. This principle is proved by Wide-angle X-ray diffraction (WAXD) and SFG results as shown in Fig. 17b and 17c. The WAXD measurement of the 20wt% CNC in PAN film show isotropic ordering as full circles appear. On the other hand, the XRD feature of

uniaxial arrangement is observed after the gel-spinning. Lower OH/CH peak ratios of SFG signal in Fig. 17c clearly shows that the polarity of hydroxyl groups in the uniaxial arrangement is much less than the random arrangement. This decreased polarity of hydroxyl groups is induced by the anti-parallel arrangement of CNCs; if they are arranged in parallel, the OH/CH peak ratio should increase (Fig. 5).[42]

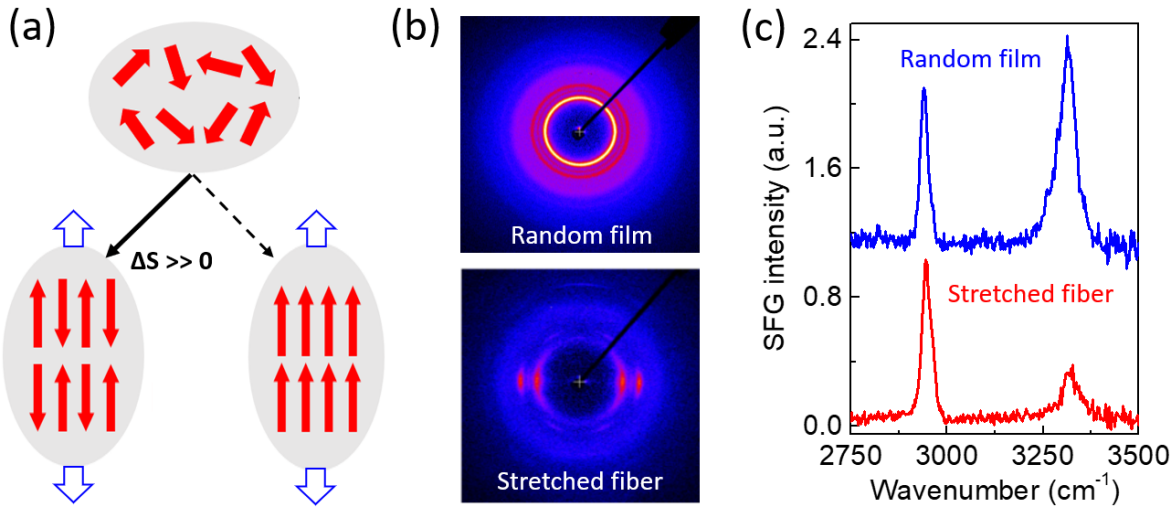

Figure 17. (a) Schematics of uniaxial, but anti-parallel arrangement (entropy increases, ΔS >0) of particles by mechanical stretching. (b) WAXD patterns of PAN/CNC 20wt% film (random) and stretched fiber (uniaxial). (c) SFG spectrum of the PAN/CNC film (random, blue) and stretched PAN/CNC fiber (anti-parallel, red).

5. Construction of nano-building blocks of CNCs with uniaxial alignment using LB deposition and investigation of their optical and frictional anisotropic properties

In this project, an effective method of structuring CNCs from a monolayer to multiple layers with the uniaxial alignment was developed using the LB deposition. Using the uniaxially aligned CNCs film, their optical and frictional anisotropic properties were also investigated. Two different orientations of fused quartz substrates in the vertical deposition were compared as shown in Fig. 18. When cationic DODA molecules are floating on the surface of water, negatively charged CNC are attracted to the air/DODA/water interface due to the electrostatic attraction.[62-63] When the substrate is perpendicular to the compressed barriers, the long axes of CNCs are aligned along the pulling direction (pink arrow) as shown in Fig. 18a. On the other hand, non-homogeneous arrangement of CNCs was observed as shown in Fig. 18b.

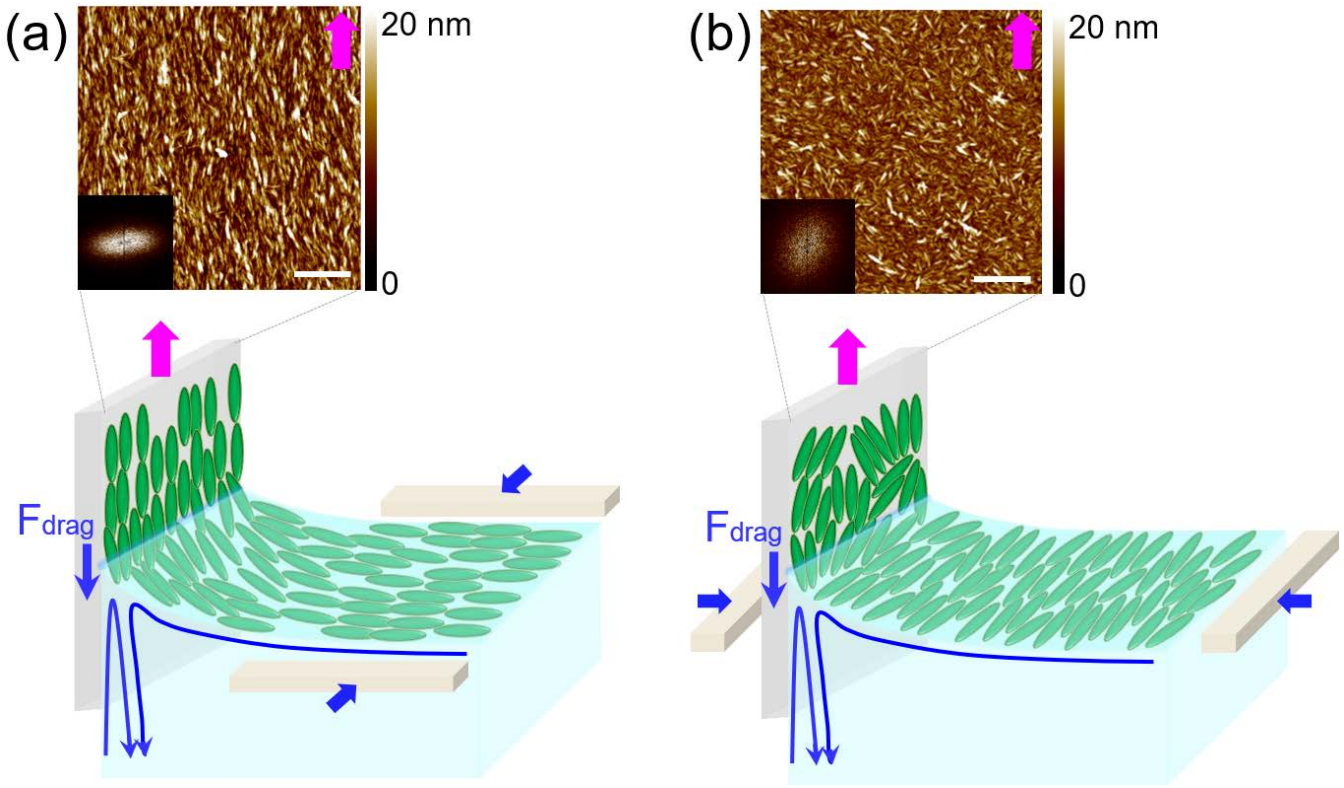

Figure 18. Comparison of the alignment of CNCs in two different orientations of substrates with respect to the barriers. The fused quartz substrate is (a) perpendicular and (b) parallel to the compressed barriers, respectively. AFM images of the deposited DODA/CNC monolayer on the substrates at 60 mN/m in case (a) and case (b). The pink arrows represent the pulling direction. The scale bars represent 1 μm.[7]

This difference between case (a) and case (b) originates from the flow-induced alignment of CNCs during the LB deposition. Before the pulling substrates, long axes of CNCs should be aligned along the barriers on the water surface. During the vertical pulling of the substrate, the flow-induced alignment of CNCs improves the compression-induced alignment in case (a) as the minimum drag force is applied when long CNCs are along the pulling direction at the water meniscus on substrate. However, it decreases in case (b) as a larger drag force is applied along the short axes of CNCs, which can reorient CNCs during the pulling deposition. This method can be used to prepare multiple layers of uniaxial CNCs. A slight decrease of anisotropic ordering was observed as the number of layers increases due to the topographic roughness.

The optical and frictional anisotropic properties of CNCs were obtained from the uniaxially aligned monolayer of DODA/CNC as shown in Fig. 19.[7] The spectroscopic ellipsometry results in Fig. 19b shows that the effective refractive index along the long axis of CNCs (n∥) is higher than that of short axis of CNCs (n⊥). The refractive index and birefringence of this this film is within the range previously

reported for cellulose.[67-69] This also proves that the uniaxial alignment of CNCs on the fused quartz substrate has macroscopic homogeneity as the probing region of ellipsometric measurement is few-mm scale. The uniaxial alignment of CNC in the LB monolayer induces an anisotropy in the friction test using AFM as shown in Fig. 19c. The nanoscale friction measurement was performed using a blunt Si tip. The result shows that the friction force along the short axis of CNCs (blue) is approximately 34% higher than that of long axis of CNCs (red). This in-plane anisotropic property must come from topography of CNCs. There are more up- and down-hills along the short axis, and this causes more up-and down-movement of the Si tip and larger friction force. The findings of this study would be widely used for constructing uniformly arranged nanoparticles in LB methods as well as quantitative measurements of the anisotropic ordering.

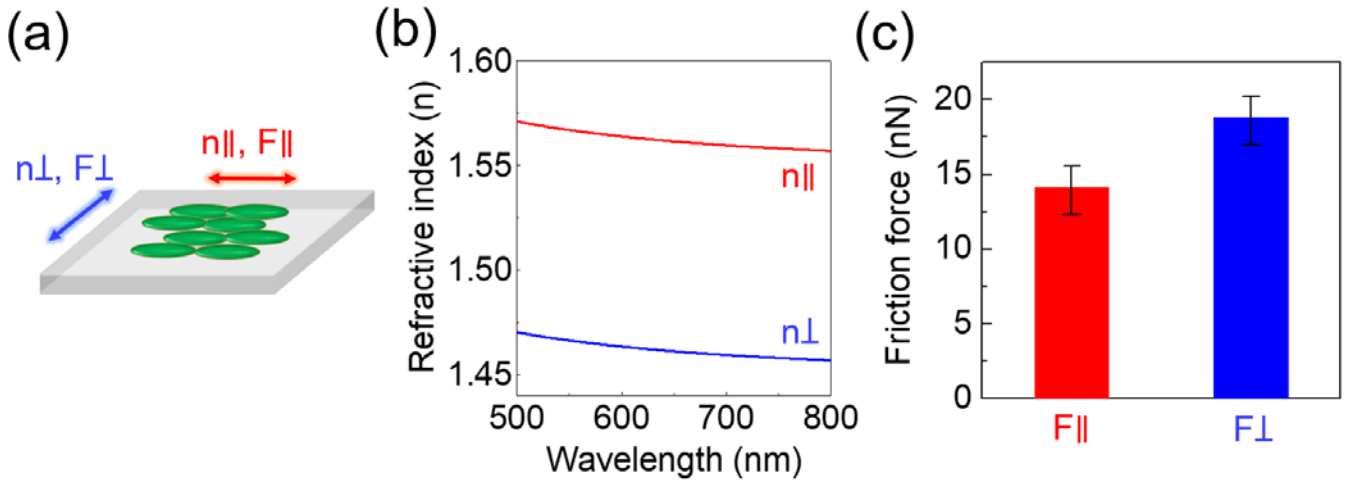

Figure 19. (a) Schematic illustration of the uniaxially aligned monolayer DODA/CNC on fused quartz. (b) Effective refractive indices and (c) friction forces of the uniaxially aligned DODA/CNCs along the long axis and short axis of the CNCs.[70]

Conclusions

Through the literature review and characterizations of cellulose-based samples such as EAPap, we found that the reported values in the previous literature are not solely from piezoelectricity. Non-piezoelectric couplings can intrinsically and extrinsically affect the piezoelectric measurements. In other words, they can contribute to the piezoelectric signals as artifacts; the measured piezoelectric signals could be outweighed by the non-piezoelectric signals. In the previous literature, various piezoelectric coefficients of cellulose-based materials over 6 orders of magnitudes have been reported. No direct evidence of their polar ordering has been reported, which makes it difficult to confirm whether the reported values are truly piezoelectric responses or not. Without knowing the origins and exact mechanisms, it is

impossible to utilize the properties. Thus, we need to focus on accurately identifying and categorizing the electromechanical properties of CNCs.

We initially hypothesized, based on the literature and our experimental work, that it is possible to align extracted CNCs in parallel by applying electric or magnetic field. CNCs have a dipole moment and diamagnetic susceptibility from the asymmetric arrangement of chains, which can react to the electric and magnetic field, respectively.[53] An important step is to find optimal field conditions to rotate them and fix their orientations uniformly. We have tested various methods; however, the parallel alignment of CNCs could not be achieved. We found that it is actually very challenging because random and anti-parallel alignments are thermodynamically more favorable than the parallel alignment case, and individually separated CNCs have net negative surface charges. In nanoscale particles, surface effects are usually dominant over bulk effects. Other approaches like functionalization of CNC reducing ends with alkyl chains and applying E-field during the curing CNCs-PDMS composite had been tried, but they were abandoned because CNCs were aggregated during the chemical functionalization process.

Dispersions of individual CNCs in polar organic solvents including DMF and NMF, and a polymer matrix (PVAC) are obtained. Also, rotational and translational behaviors of CNCs under external forces are systematically studied. Under electric field, CNCs can rotate with their permanent dipole moment; however, this bulk effect is difficult to observe due to the electrophoretic translation (surface effect). Under magnetic field and high concentration in liquid, CNCs can form a chiral nematic phase. CNCs are arranged as opposite to neighboring CNCs in average during this chiral nematic phase formation; i.e., reducing end to non-reducing end. Mechanical compression and stretching of randomly arranged CNCs induce uniaxial, but anti-parallel arrangements. In addition, the unique ability of SFG to characterize the polar ordering of PVDF and cellulose has been identified in our studies.[2, 42] Finally, SFG microscopy system was built in our lab, and we could analyze the orientations of CNCs in microscopic regions. This system also allows the scanning SFG signals over microscopic areas with the translational stage. This advanced technique will be further used for the characterization of polar ordering in not only cellulose, but also other biomaterials such as chitin and collagen.

There are other tasks that we would like to perform with renewing this project. Our collaborator, Dr. Ogawa found that *Lamellibrachia Satsuma* tubeworms living near hydrothermal vents at the sea floor has naturally arranged β-chitin in parallel fashion.[71] Due to the parallel arrangement of β-chitin (unipolar), this sample is an ideal candidate to identify the relationship between piezoelectricity and polar ordering. Chitin has similar crystalline structures to cellulose. We are currently testing this sample using nonlinear

optical spectroscopy and piezo-response force microscopy (PFM). Using PFM, a small piezoelectric signal such as few- or sub-pm/V can be detected. In addition, we are planning to try a rotating magnetic field for the alignments of CNCs. It has been found that rotating magnetic field can un-roll chiral assembly of CNCs.[72] We plan to investigate this behavior of CNCs under rotating magnetic field as well as the polar ordering of this un-rolled CNC films. On top of that, to induce the polar ordering of CNCs, more approaches of chemically decorating reducing ends of CNCs would be made.

References

1. Chae, I.; Jeong, C. K.; Ounaies, Z.; Kim, S. H., Review on Electromechanical Coupling Properties of Biomaterials. *ACS Applied Bio Materials* **2018,** *1* (4), 936-953.
2. Chae, I.; Ahmed, S.; Atitallah, H. B.; Luo, J.; Wang, Q.; Ounaies, Z.; Kim, S. H., Vibrational Sum Frequency Generation (SFG) Analysis of Ferroelectric Response of Pvdf-Based Copolymer and Terpolymer. *Macromolecules* **2017,** *50* (7), 2838-2844.
3. Lee, C. M.; Chen, X.; Weiss, P. A.; Jensen, L.; Kim, S. H., Quantum Mechanical Calculations of Vibrational Sum-Frequency-Generation (SFG) Spectra of Cellulose: Dependence of the Ch and Oh Peak Intensity on the Polarity of Cellulose Chains within the SFG Coherence Domain. *J. Phys. Chem. Lett.* **2017,** *8* (1), 55-60.
4. Chae, I.; Ngo, D.; Makarem, M.; Ounaies, Z.; Kim, S. H., Compression-Induced Topographic Corrugation of Air/Surfactant/Water Interface: Effect of Nanoparticles Adsorbed beneath the Interface. *Under revision in J. Phys. Chem. C* **2019**.
5. Meddeb, A.; Chae, I.; Aijie, H.; Kim, S. H.; Ounaies, Z., Solvent Properties, Particle Content and Magnetic Field Effects on Cellulose Nanocrystals Packing in Suspensions. *Submitted to ACS Applied Bio Materials* **2019**.
6. Meddeb, A. B.; Chae, I.; Kim, S. H.; Ounaies, Z., Enhanced Antiparallel Packing of Cellulose Nanocrystals by Magnetic Field Application. *Manuscript in preparation* **2019**.
7. Chae, I.; Ngo, D.; Chen, Z.; Meddeb, A. B.; Kwansa, A.; Podraza, N. J.; Yingling, Y. G.; Ounaies, Z.; Kim, S. H., Structuring of Rod-Shaped Nanoparticles in Langmuir-Blodgett Film: Effect of Uniaxial Alignment of Optical and Frictional Anisotropy. *Submitted to ACS Applied Materials & Interfaces* **2019**.
8. Rajala, S.; Siponkoski, T.; Sarlin, E.; Mettanen, M.; Vuoriluoto, M.; Pammo, A.; Juuti, J.; Rojas, O. J.; Franssila, S.; Tuukkanen, S., Cellulose Nanofibril Film as a Piezoelectric Sensor Material. *ACS Appl Mater Interfaces* **2016,** *8* (24), 15607-14.
9. Alam, M. M.; Mandal, D., Native Cellulose Microfiber-Based Hybrid Piezoelectric Generator for Mechanical Energy Harvesting Utility. *ACS Appl Mater Interfaces* **2016,** *8* (3), 1555-8.
10. Mahadeva, S. K.; Walus, K.; Stoeber, B., Piezoelectric Paper Fabricated Via Nanostructured Barium Titanate Functionalization of Wood Cellulose Fibers. *ACS Appl Mater Interfaces* **2014,** *6* (10), 7547-53.
11. Csoka, L.; Hoeger, I. C.; Rojas, O. J.; Peszlen, I.; Pawlak, J. J.; Peralta, P. N., Piezoelectric Effect of Cellulose Nanocrystals Thin Films. *ACS Macro Letters* **2012,** *1* (7), 867-870.
12. Hirai, N.; Sobue, N.; Date, M., New Piezoelectric Moduli of Wood: D 31 and D 32. *Journal of Wood Science* **2010,** *57* (1), 1-6.
13. Gindl, W.; Emsenhuber, G.; Plackner, J.; Konnerth, J.; Keckes, J., Converse Piezoelectric Effect in Cellulose I Revealed by Wide-Angle X-Ray Diffraction. *Biomacromolecules* **2010,** *11* (5), 1281-1285.
14. Yang, C.; Kim, J.-H.; Kim, J.-H.; Kim, J.; Kim, H. S., Piezoelectricity of Wet Drawn Cellulose Electro-Active Paper. *Sensors and Actuators A: Physical* **2009,** *154* (1), 117-122.
15. Kim, J., Improvement of Piezoelectricity in Piezoelectric Paper Made with Cellulose. *AOARD-084035* **2009**.

16. Yun, S.; Jang, S.; Yun, G.-Y.; Kim, J., Electrically Aligned Cellulose Film for Electro-Active Paper and Its Piezoelectricity. *Smart Mater. Struct.* **2009,** *18* (11), 117001.
17. Yun, S.; Kim, J. H.; Li, Y.; Kim, J., Alignment of Cellulose Chains of Regenerated Cellulose by Corona Poling and Its Piezoelectricity. *Journal of Applied Physics* **2008,** *103* (8), 083301.
18. Yun, G. Y.; Kim, H. S.; Kim, J.; Kim, K.; Yang, C., Effect of Aligned Cellulose Film to the Performance of Electro-Active Paper Actuator. *Sensors and Actuators A: Physical* **2008,** *141* (2), 530-535.
19. Fukada, E.; Date, M.; Hirai, N., Effect of Temperature on Piezoelectricity in Wood. *Journal of Polymer Science Part C: Polymer Symposia* **1968,** *23* (2), 509-517.
20. Fukada, E., Piezoelectricity as a Fundamental Property of Wood. *Wood Science and Technology* **1968,** *2* (4), 299-307.
21. Eiichi, F.; Iwao, Y., Piezoelectric Effects in Collagen. *Japanese Journal of Applied Physics* **1964,** *3* (2), 117.
22. Halperin, C.; Mutchnik, S.; Agronin, A.; Molotskii, M.; Urenski, P.; Salai, M.; Rosenman, G., Piezoelectric Effect in Human Bones Studied in Nanometer Scale. *Nano Letters* **2004,** *4* (7), 1253-1256.
23. Lee, B. Y.; Zhang, J.; Zueger, C.; Chung, W. J.; Yoo, S. Y.; Wang, E.; Meyer, J.; Ramesh, R.; Lee, S. W., Virus-Based Piezoelectric Energy Generation. *Nat Nanotechnol* **2012,** *7* (6), 351-6.
24. Shin, D.-M.; Han, H. J.; Kim, W.-G.; Kim, E.; Kim, C.; Hong, S. W.; Kim, H. K.; Oh, J.-W.; Hwang, Y.-H., Bioinspired Piezoelectric Nanogenerators Based on Vertically Aligned Phage Nanopillars. *Energy Environ. Sci.* **2015,** *8* (11), 3198-3203.
25. Ghosh, S. K.; Mandal, D., Efficient Natural Piezoelectric Nanogenerator: Electricity Generation from Fish Swim Bladder. *Nano Energy* **2016,** *28*, 356-365.
26. Jayasuriya, A. C.; Ghosh, S.; Scheinbeim, J. I.; Lubkin, V.; Bennett, G.; Kramer, P., A Study of Piezoelectric and Mechanical Anisotropies of the Human Cornea. *Biosensors and Bioelectronics* **2003,** *18* (4), 381-387.
27. Fukada, E.; Yasuda, I., On the Piezoelectric Effect of Bone. *Journal of the Physical Society of Japan* **1957,** *12* (10), 1158-1162.
28. Yucel, T.; Cebe, P.; Kaplan, D. L., Structural Origins of Silk Piezoelectricity. *Adv Funct Mater* **2011,** *21* (4), 779-785.
29. Fukada, E., History and Recent Progress in Piezoelectric Polymers. *IEEE Transactions on Ultrasonics, Ferroelectrics, and Frequency Control* **2000,** *47* (6), 1277-1290.
30. Minary-Jolandan, M.; Yu, M.-F., Shear Piezoelectricity in Bone at the Nanoscale. *Applied Physics Letters* **2010,** *97* (15), 153127.
31. Minary-Jolandan, M.; Yu, M. F., Nanoscale Characterization of Isolated Individual Type I Collagen Fibrils: Polarization and Piezoelectricity. *Nanotechnology* **2009,** *20* (8), 085706.
32. Minary-Jolandan, M.; Yu, M.-F., Uncovering Nanoscale Electromechanical Heterogeneity in the Subfibrillar Structure of Collagen Fibrils Responsible for the Piezoelectricity of Bone. *ACS Nano* **2009,** *3* (7), 1859-1863.
33. Karan, S. K.; Maiti, S.; Kwon, O.; Paria, S.; Maitra, A.; Si, S. K.; Kim, Y.; Kim, J. K.; Khatua, B. B., Nature Driven Spider Silk as High Energy Conversion Efficient Bio-Piezoelectric Nanogenerator. *Nano Energy* **2018**.
34. Stapleton, A.; Noor, M. R.; Sweeney, J.; Casey, V.; Kholkin, A. L.; Silien, C.; Gandhi, A. A.; Soulimane, T.; Tofail, S. A. M., The Direct Piezoelectric Effect in the Globular Protein Lysozyme. *Applied Physics Letters* **2017,** *111* (14), 142902.
35. Liu, Y.; Wang, Y.; Chow, M.-J.; Chen, N. Q.; Ma, F.; Zhang, Y.; Li, J., Glucose Suppresses Biological Ferroelectricity in Aortic Elastin. *Physical Review Letters* **2013,** *110* (16), 168101.
36. Eiichi, F.; Hiroyoshi, U., Piezoelectric Effect in Muscle. *Japanese Journal of Applied Physics* **1970,** *9* (7), 844.
37. Hiroyoshi, U.; Eiichi, F., Piezoelectricity in Myosin and Actin. *Japanese Journal of Applied Physics* **1971,** *10* (11), 1650.
38. Fukada, E.; Zimmerman, R. L.; Mascarenhas, S., Denaturation of Horn Keratin Observed by Piezoelectric Measurements. *Biochemical and Biophysical Research Communications* **1975,** *62* (2), 415-418.
39. Dragan, D., Ferroelectric, Dielectric and Piezoelectric Properties of Ferroelectric Thin Films and Ceramics. *Reports on Progress in Physics* **1998,** *61* (9), 1267.

40. Lovinger, A. J., Ferroelectric Polymers. *Science* **1983,** *220* (4602), 1115-1121.
41. Kepler, R. G.; Anderson, R. A., Ferroelectricity in Polyvinylidene Fluoride. *Journal of Applied Physics* **1978,** *49* (3), 1232-1235.
42. Chen, X.; Lee, C. M.; Wang, H.-F.; Jensen, L.; Kim, S. H., Experimental and Theoretical Study of Azimuth Angle and Polarization Dependences of Sum-Frequency-Generation Vibrational Spectral Features of Uniaxially Aligned Cellulose Crystals. *The Journal of Physical Chemistry C* **2017,** *121* (34), 18876-18886.
43. Lee, C. M.; Mittal, A.; Barnette, A. L.; Kafle, K.; Park, Y. B.; Shin, H.; Johnson, D. K.; Park, S.; Kim, S. H., Cellulose Polymorphism Study with Sum-Frequency-Generation (SFG) Vibration Spectroscopy: Identification of Exocyclic Ch2oh Conformation and Chain Orientation. *Cellulose* **2013,** *20* (3), 991-1000.
44. Kim, J.; Yun, G.-Y.; Kim, J.-H.; Lee, J.; Kim, J.-H., Piezoelectric Electro-Active Paper (Eapap) Speaker. *Journal of Mechanical Science and Technology* **2011,** *25* (11), 2763-2768.
45. Kim, J.; Lee, H.; Kim, H. S.; Kim, J., Vibration Sensor Characteristics of Piezoelectric Electro-Active Paper. *Journal of Intelligent Material Systems and Structures* **2010,** *21* (11), 1123-1130.
46. Barnette, A. L.; Bradley, L. C.; Veres, B. D.; Schreiner, E. P.; Park, Y. B.; Park, J.; Park, S.; Kim, S. H., Selective Detection of Crystalline Cellulose in Plant Cell Walls with Sum-Frequency-Generation (SFG) Vibration Spectroscopy. *Biomacromolecules* **2011,** *12* (7), 2434-2439.
47. Garcia, Y.; Ruiz-Blanco, Y. B.; Marrero-Ponce, Y.; Sotomayor-Torres, C. M., Orthotropic Piezoelectricity in 2d Nanocellulose. *Sci Rep* **2016,** *6*, 34616.
48. Kim, S.; Choi, S. J.; Zhao, K.; Yang, H.; Gobbi, G.; Zhang, S.; Li, J., Electrochemically Driven Mechanical Energy Harvesting. *Nat Commun* **2016,** *7*, 10146.
49. Kim, J.; Montero, G.; Habibi, Y.; Hinestroza, J. P.; Genzer, J.; Argyropoulos, D. S.; Rojas, O. J., Dispersion of Cellulose Crystallites by Nonionic Surfactants in a Hydrophobic Polymer Matrix. *Polymer Engineering & Science* **2009,** *49* (10), 2054-2061.
50. Heux, L.; Chauve, G.; Bonini, C., Nonflocculating and Chiral-Nematic Self-Ordering of Cellulose Microcrystals Suspensions in Nonpolar Solvents. *Langmuir* **2000,** *16* (21), 8210-8212.
51. Csoka, L.; Hoeger, I. C.; Peralta, P.; Peszlen, I.; Rojas, O. J., Dielectrophoresis of Cellulose Nanocrystals and Alignment in Ultrathin Films by Electric Field-Assisted Shear Assembly. *Journal of Colloid and Interface Science* **2011,** *363* (1), 206-212.
52. Habibi, Y.; Heim, T.; Douillard, R., Ac Electric Field-Assisted Assembly and Alignment of Cellulose Nanocrystals. *Journal of Polymer Science Part B: Polymer Physics* **2008,** *46* (14), 1430-1436.
53. Bruno, F.-P.; Bruno, J.; Laurent, H., First Experimental Evidence of a Giant Permanent Electric-Dipole Moment in Cellulose Nanocrystals. *EPL (Europhysics Letters)* **2014,** *107* (2), 28006.
54. Habibi, Y.; Lucia, L. A.; Rojas, O. J., Cellulose Nanocrystals: Chemistry, Self-Assembly, and Applications. *Chemical Reviews* **2010,** *110* (6), 3479-3500.
55. Chae, I.; Meddeb, A.; Ounaies, Z.; Kim, S. H., Tailoring and Characterization of the Liquid Crystalline Structure of Cellulose Nanocrystals for Opto-Electro-Mechanical Multifunctional Applications. **2018,** (51944), V001T01A010.
56. Chen, Q.; de Larraya, U. P.; Garmendia, N.; Lasheras-Zubiate, M.; Cordero-Arias, L.; Virtanen, S.; Boccaccini, A. R., Electrophoretic Deposition of Cellulose Nanocrystals (Cns) and Cns/Alginate Nanocomposite Coatings and Free Standing Membranes. *Colloids and Surfaces B: Biointerfaces* **2014,** *118* (Supplement C), 41-48.
57. Pan, J.; Hamad, W.; Straus, S. K., Parameters Affecting the Chiral Nematic Phase of Nanocrystalline Cellulose Films. *Macromolecules* **2010,** *43* (8), 3851-3858.
58. Tardy, B. L.; Ago, M.; Guo, J.; Borghei, M.; Kämäräinen, T.; Rojas, O. J., Optical Properties of Self-Assembled Cellulose Nanocrystals Films Suspended at Planar–Symmetrical Interfaces. *Small* **2017,** *13* (47), 1702084.
59. Frka-Petesic, B.; Sugiyama, J.; Kimura, S.; Chanzy, H.; Maret, G., Negative Diamagnetic Anisotropy and Birefringence of Cellulose Nanocrystals. *Macromolecules* **2015,** *48* (24), 8844-8857.

60. De France, K. J.; Chan, K. J. W.; Cranston, E. D.; Hoare, T., Enhanced Mechanical Properties in Cellulose Nanocrystal–Poly(Oligoethylene Glycol Methacrylate) Injectable Nanocomposite Hydrogels through Control of Physical and Chemical Cross-Linking. *Biomacromolecules* **2016,** *17* (2), 649-660.
61. Lee, C. M.; Chen, X.; Weiss, P. A.; Jensen, L.; Kim, S. H., Quantum Mechanical Calculations of Vibrational Sum-Frequency-Generation (SFG) Spectra of Cellulose: Dependence of the Ch and Oh Peak Intensity on the Polarity of Cellulose Chains within the SFG Coherence Domain. *The Journal of Physical Chemistry Letters* **2017,** *8* (1), 55-60.
62. Habibi, Y.; Hoeger, I.; Kelley, S. S.; Rojas, O. J., Development of Langmuir−Schaeffer Cellulose Nanocrystal Monolayers and Their Interfacial Behaviors. *Langmuir* **2010,** *26* (2), 990-1001.
63. Habibi, Y.; Foulon, L.; Aguié-Béghin, V.; Molinari, M.; Douillard, R., Langmuir–Blodgett Films of Cellulose Nanocrystals: Preparation and Characterization. *Journal of Colloid and Interface Science* **2007,** *316* (2), 388-397.
64. Yan, E. C. Y.; Fu, L.; Wang, Z.; Liu, W., Biological Macromolecules at Interfaces Probed by Chiral Vibrational Sum Frequency Generation Spectroscopy. *Chemical Reviews* **2014,** *114* (17), 8471-8498.
65. Makarem, M.; Sawada, D.; O'Neill, H. M.; Lee, C. M.; Kafle, K.; Park, Y. B.; Mittal, A.; Kim, S. H., Dependence of Sum Frequency Generation (SFG) Spectral Features on the Mesoscale Arrangement of SFG-Active Crystalline Domains Interspersed in SFG-Inactive Matrix: A Case Study with Cellulose in Uniaxially Aligned Control Samples and Alkali-Treated Secondary Cell Walls of Plants. *The Journal of Physical Chemistry C* **2017,** *121* (18), 10249-10257.
66. Chang, H.; Chien, A.-T.; Liu, H. C.; Wang, P.-H.; Newcomb, B. A.; Kumar, S., Gel Spinning of Polyacrylonitrile/Cellulose Nanocrystal Composite Fibers. *ACS Biomaterials Science & Engineering* **2015,** *1* (7), 610-616.
67. Klemm, D.; Philpp, B.; Heinze, T.; Heinze, U.; Wagenknecht, W., *Comprehensive Cellulose Chemistry. Volume 1: Fundamentals and Analytical Methods*. Wiley-VCH Verlag GmbH: Weinheim, 1998; p xxii + 260 pp.
68. Cranston, E. D.; Gray, D. G., Birefringence in Spin-Coated Films Containing Cellulose Nanocrystals. *Colloids and Surfaces A: Physicochemical and Engineering Aspects* **2008,** *325* (1), 44-51.
69. Karabiyik, U.; Mao, M.; Roman, M.; Jaworek, T.; Wegner, G.; Esker, A. R., Optical Characterization of Cellulose Films Via Multiple Incident Media Ellipsometry. In *Model Cellulosic Surfaces*, American Chemical Society: 2009; Vol. 1019, pp 137-155.
70. Chae, I.; Ngo, D.; Chen, Z.; Meddeb, A.; Kwansa, A.; Podraza, N. J.; Yingling, Y. G.; Ounaies, Z.; Kim, S. H., Structuring of Rod-Shaped Nanoparticles in the Langmuir-Blodgett Films: Effect of Uniaxial Alignment on Their Optical and Frictional Anisotropy. *Unpublished* **2019**.
71. Ogawa, Y.; Kobayashi, K.; Kimura, S.; Nishiyama, Y.; Wada, M.; Kuga, S., X-Ray Texture Analysis Indicates Downward Spinning of Chitin Microfibrils in Tubeworm Tube. *Journal of Structural Biology* **2013,** *184* (2), 212-216.
72. Kimura, F.; Kimura, T.; Tamura, M.; Hirai, A.; Ikuno, M.; Horii, F., Magnetic Alignment of the Chiral Nematic Phase of a Cellulose Microfibril Suspension. *Langmuir* **2005,** *21* (5), 2034-2037.